Mechanics of spontaneously formed nanoblisters trapped by transferred 2D crystals

Daniel A. Sanchez[a,1], Zhaohe Dai[b,1], Peng Wang[b], Arturo Cantu-Chavez[a], Christopher J. Brennan[c], Rui Huang[a,b,2], and Nanshu Lu[a,b,c,d,2]

[a]Texas Materials Institute, The University of Texas at Austin, Austin, TX 78712; [b]Department of Aerospace Engineering and Engineering Mechanics, Center for Mechanics of Solids, Structures and Materials, The University of Texas at Austin, Austin, TX 78712; [c]Department of Electrical and Computer Engineering, The University of Texas at Austin, Austin, TX 78712; and [d]Department of Biomedical Engineering, The University of Texas at Austin, Austin, TX 78712

Edited by John A. Rogers, Northwestern University, Evanston, IL, and approved June 21, 2018 (received for review January 26, 2018)

Layered systems of 2D crystals and heterostructures are widely explored for new physics and devices. In many cases, monolayer or few-layer 2D crystals are transferred to a target substrate including other 2D crystals, and nanometer-scale blisters form spontaneously between the 2D crystal and its substrate. Such nanoblisters are often recognized as an indicator of good adhesion, but there is no consensus on the contents inside the blisters. While gas-filled blisters have been modeled and measured by bulge tests, applying such models to spontaneously formed nanoblisters yielded unrealistically low adhesion energy values between the 2D crystal and its substrate. Typically, gas-filled blisters are fully deflated within hours or days. In contrast, we found that the height of the spontaneously formed nanoblisters dropped only by 20–30% after 3 mo, indicating that probably liquid instead of gas is trapped in them. We therefore developed a simple scaling law and a rigorous theoretical model for liquid-filled nanoblisters, which predicts that the interfacial work of adhesion is related to the fourth power of the aspect ratio of the nanoblister and depends on the surface tension of the liquid. Our model was verified by molecular dynamics simulations, and the adhesion energy values obtained for the measured nanoblisters are in good agreement with those reported in the literature. This model can be applied to estimate the pressure inside the nanoblisters and the work of adhesion for a variety of 2D interfaces, which provides important implications for the fabrication and deformability of 2D heterostructures and devices.

2D materials | heterostructures | nanoblisters | adhesion | membrane theory

Two-dimensional (2D) crystals are atomically thin, layered materials with strong bonding in the crystal plane and weak bonding via van der Waals (vdW) interactions between the layers (1, 2). Discovery of 2D crystals has fueled extensive fundamental and applied research due to their remarkable electronic, mechanical, optical, and magnetic properties. Rapidly emerging experimental and modeling results indicate that mechanical strains can strongly perturb the band structure of 2D crystals (3–5). In the nanoscale regime, the vdW interactions between the monolayer 2D crystal and its substrate can have strong influences on the mechanical behavior of 2D materials (6–8). Consequently, the performance of 2D-crystal–based devices relies heavily on the vdW interfaces. In reality, however, the vdW attraction between the 2D crystal and its substrate may cause adsorbed ambient molecules to lump together in the interface, resulting in micro- or nanoblisters which often degrade device performance (9, 10). Interfacial blisters are also frequently seen in vdW heterostructures (i.e., stacks of 2D crystals), causing significant charge inhomogeneity and limiting the carrier mobilities of a device (1, 2). Alternatively, due to the strong electromechanical coupling, nanoblisters have been applied for strain engineering of 2D materials (5, 11). Moreover, interface-confined chemistry was explored within 2D material blisters leveraging their high internal pressure (12–19). To either control or avoid blisters for the 2D materials, it is imperative to understand the formation mechanism for these nanoblisters and reveal the key parameters.

Many studies have been carried out recently to explore various aspects of nanoblisters, including the effects of heat (10), blister content (12), humidity dependence (20), and their shape characteristics (13). Although there is no consensus on whether the blisters are filled with air, liquid, or solid (21, 22), adhesion is one of the well-accepted governing parameters for the formation of blisters. In fact, interfacial blisters have been used as indicators of good adhesion between the constituents of vdW heterostructures (1), since blisters are energetically favorable only when the adhesion between layers is relatively high. Mechanics models have been developed and widely used to relate gas-filled blister profiles to interfacial adhesion (12, 20, 23–25). However, the subtle nature of the content inside the blisters may render the assumption of a gas content inappropriate. Direct application of this ad hoc model has led to unrealistically small adhesion values for graphene interfaces compared with well-established adhesion measurements (20).

In this work, we tracked the height of graphene blisters on SiO_2 over the course of 3 mo. Extremely slow deflation of the blisters was observed, indicating that they are likely filled with liquid instead of gas content. We therefore developed a scaling law and a more rigorous analytical model based on the elastic

Significance

Spontaneously formed nanoblisters are almost inevitable when transferring 2D crystals to a substrate. We hypothesize that those nanoblisters are filled with liquid according to our time-lapse atomic force microscopy scans and reasonable estimation of adhesion energy. We show that the liquid-filled nanoblisters form as a result of competition between the elastic energy of the deformed 2D crystal, the interfacial energy associated with van der Waals interactions, and surface tension of the liquid contents. Besides pointing to solutions for controlling their shape and internal pressure, our analysis provides a method to estimate the work of adhesion of 2D material interfaces by simply measuring the aspect ratios of the blisters, which is essential for the design and fabrication of 2D crystal-based applications.

Author contributions: N.L. designed research; D.A.S., Z.D., P.W., A.C.-C., and C.J.B. performed research; D.A.S., Z.D., P.W., A.C.-C., C.J.B., R.H., and N.L. analyzed data; and D.A.S., Z.D., P.W., R.H., and N.L. wrote the paper.

The authors declare no conflict of interest.

This article is a PNAS Direct Submission.

[1]D.A.S. and Z.D. contributed equally to this work.

[2]To whom correspondence may be addressed. Email: ruihuang@mail.utexas.edu or nanshulu@utexas.edu.

This article contains supporting information online at www.pnas.org/lookup/suppl/doi:10.1073/pnas.1801551115/-/DCSupplemental.

membrane theory for liquid-filled nanoblisters. Compared with gas-filled blisters assuming ideal gas law for the content, the liquid blister theory assumes that the liquid inside the blister is nearly incompressible. However, the shape characteristics of the blister may vary depending on how the liquid interacts with the membrane and the substrate. Our analytical model is then compared with molecular dynamics (MD) simulations to provide a verification from the atomistic level. Like the gas blister theory, our liquid blister theory can also be utilized to quantitatively characterize the adhesion properties for the 2D materials based on the measured blister profiles. Alternatively, the blister shape, strain, and pressure characteristics can be controlled by tuning adhesion properties and trapped contents, which provides a viable guideline for the design of 2D material blisters for various applications.

Results

Shape Characteristics of Blisters. In this work, our experiments focus on the characteristics of nanoblisters that form at the graphene–SiO_2 and 2D MoS_2–SiO_2 interfaces, as graphene and MoS_2 are two of the most prevalent 2D materials so far. Additionally, we find blisters that form when chemical-vapor–deposited MoS_2 is transferred to Al_2O_3. After mechanically exfoliating highly ordered pyrolytic graphite (HOPG) onto silicon wafer with native SiO_2 (26), we identified single-layer graphene (SLG) areas that show a remarkably large number of blisters (Fig. 1*A*). The same procedure was also used to exfoliate 2D MoS_2 flakes from its bulk crystal onto SiO_2 (*SI Appendix*, Fig. S1*B*). For both samples, monolayer regions were identified using Raman spectroscopy (*SI Appendix*, Fig. S1) (27). Blisters trapped by SLG and few-layer graphene (FLG) in the optical micrograph appear as light-blue, circular regions, and are scattered throughout the flake (Fig. 1*A*, *Inset*). Using tapping-mode atomic force microscopy (AFM) (Fig. 1*B*), we can obtain the height profiles of the blisters. We denote the center height of the blister by h and its radius by a, such that the aspect ratio is given as h/a. The height and radius of the blisters are calculated by curve-fitting the assumed deflection profile for a pressurized membrane,

$$w(r) = h\left(1 - \frac{r^2}{a^2}\right), \quad [1]$$

to the measured data (Fig. 1*C*). Further information on the experimental procedure for creating and characterizing blisters is provided in *SI Appendix*, section 1. To use the aspect ratio of a blister as a characterization method, the in-plane shape of the blister should be approximately circular such that the aspect ratio is reasonably consistent (see *SI Appendix*, section 1 for more information on the characterization of the nanoblister ellipticity). The shape of the blister may become distorted due to its local environment, causing the aspect ratio to become anisotropic. For example, in Fig. 1*B* blisters near the edges of graphene are elongated in the direction parallel to the edge leading to an elliptical instead of circular shape. Blisters with an elliptical shape can also be found along step edges in the FLG areas.

Focusing on approximately circular blisters, the measured height vs. radius in Fig. 1*D* suggests that the aspect ratios of each type of the blisters are independent of the volume of the blister, with an average aspect ratio (h/a) of 0.049 ± 0.003 for the graphene–SiO_2 blisters, 0.046 ± 0.004 for the MoS_2–SiO_2 blisters, and 0.083 ± 0.016 for the MoS_2–Al_2O_3 blisters. A constant aspect ratio for a given 2D crystal–substrate pair has also been observed for other blisters reported in the literature (13, 20), indicating that the blister aspect ratio is a key dimensionless parameter for the material system.

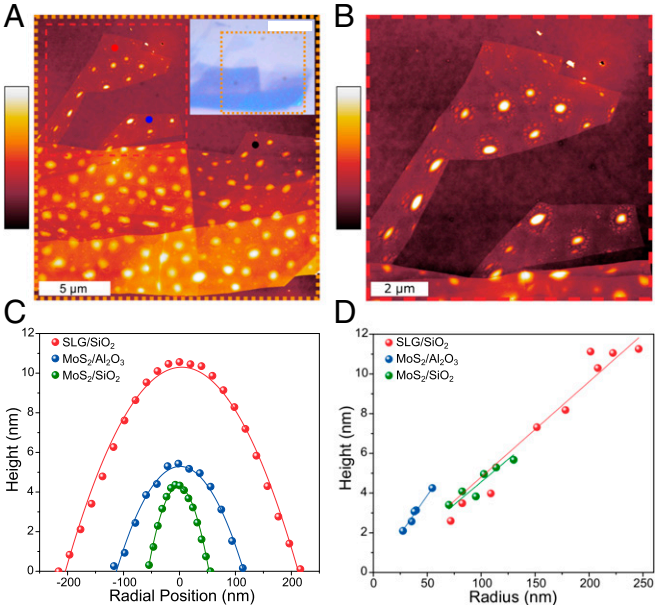

Fig. 1. Interfacial blisters between 2D crystals and their supporting substrates. (*A*) Tapping-mode AFM reveals the complex distribution of HOPG-SiO_2 blisters. (*Inset*) Bright-field optical micrograph where the orange dashed region corresponds with the large AFM image. (White scale bar: 10 μm.) The red, blue, and black dots indicate where Raman measurements were taken for *SI Appendix*, Fig. S2*A*. The color bar represents 0–17 nm. (*B*) A closer look at two monolayer regions from the red dashed region of Fig. 1*A*. Blisters close to the edges of the graphene are distorted from the typical circular shape. The color bar represents 0–13 nm. (*C*) By extracting the height profile of each blister, the height and radius is calculated by curve fitting a parabolic function. (*D*) Blisters for a specific interface show a consistent aspect ratio that is independent of volume.

Evidence of Confined Liquid. The mechanical behavior of the blister is not only dictated by the 2D crystal–substrate interaction, but also by the interactions between the trapped content and the 2D crystal/substrate. However, so far there is no consensus or direct measurement of the blister content. While several previous studies applied the gas models to analyze those blisters (12, 20, 23, 28, 29), Geim and coworkers (13, 21) strongly advocated that the blisters are filled with hydrocarbons and liquid water. Emerging observations in literature imply that the blister content is likely to be water because those blisters are found to be highly dependent on temperature (especially beyond 100 °C) and humidity (10, 20). For example, Cao et al. (22) noted that the number density and size of blisters at the graphene–HOPG interface were reduced when exfoliation was carried out in a low-humidity environment compared with exfoliation in ambient conditions. In another case, Pizzocchero et al. (10) demonstrated that blister-free interfaces for heterostructures are possible only when the 2D crystal is transferred at 110 °C, and suggested adsorbed water is the most likely candidate for the contents of the interfacial blisters.

Here we monitor the time-dependent behavior of a selected number of blisters from Fig. 1*A*. As noted in previous studies, graphene–SiO_2 interfacial blisters pressurized with gas typically deflate within 10 h for H_2-filled blisters, and 7 d for N_2-filled blisters (30–32). Since graphene is impermeable to even the smallest gas molecules (33), it was concluded that the majority of the gas content inside the blister escaped through the graphene–SiO_2 interface. Over a period of 92 d, we performed AFM scans over the same sample using consistent scanning parameters and cantilever tips. Our data show that the blisters in the SLG regions exhibit deflation at different rates, with some showing little overall change in their height (Fig. 2), which is drastically different from the time-dependent behaviors of gas blisters. Hence

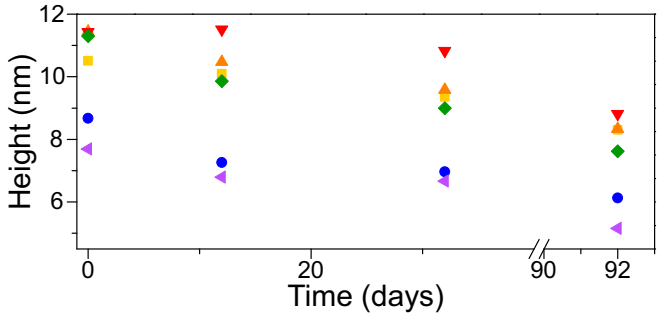

Fig. 2. Height measurements of SLG nanoblisters measured over a period of 92 d. All blisters show signs of gradual deflation, which indicates that the contents of the blister can escape through the SLG–SiO_2 interface, but at a much slower rate than trapped gas molecules.

our experiment offers evidence against the possibility of gas inside the blisters. We therefore suggest that the content inside the blisters is mostly liquid water, likely mixed with a certain amount of hydrocarbon contaminants. Following such hypothesis, in the following we present a liquid-filled blister model and adopt water as the most likely representative liquid for quantitative analysis.

Modeling. Although 2D crystals are atomically thin membranes, continuum mechanics has proven to be applicable when bending is negligible (34–36). We therefore employ an elastic membrane model to establish a direct relation between the aspect ratio of the blister and the material properties of the 2D membrane and substrate. Unlike gas-filled blisters considered in previous works (23, 29), where the ideal gas law was used to relate the pressure to the blister volume, we assume that the liquid inside the blister is nearly incompressible, but the aspect ratio (h/a) may vary depending on how the liquid interacts with the membrane and the substrate. We begin by using a simple scaling approach for determining the properties of axisymmetric blisters. The membrane over a liquid-filled blister of radius a and height h at its center is subject to a stretching strain $\varepsilon \propto h^2/a^2$ from elementary geometry. With an in-plane elastic stiffness E_{2D}, the stretching energy in the membrane scales as $U_e \propto E_{2D}\varepsilon^2 a^2 \propto E_{2D}h^4/a^2$. The bending energy of the membrane is negligible due to the thinness of the 2D membrane and relatively small aspect ratios. The adhesion energy required to form the blister is simply the energy change per unit area, $\Delta\gamma$, multiplied by the blister area, which scales as $U_i \propto \Delta\gamma a^2$. If the volume of liquid ($V \propto a^2 h$) remains a constant in the blister, the elastic energy decreases and the interfacial energy increases with increasing a. The competition leads to an equilibrium blister radius that minimizes the total free energy ($U_e + U_i$), with $h/a \propto (\Delta\gamma/E_{2D})^{1/4}$. The scaling relation for the aspect ratio (h/a) is identical to that for gas-filled blisters (23, 29). However, the change of interfacial energy is different. For a gas-filled blister, $\Delta\gamma$ is simply taken as the adhesion energy between the membrane and the substrate ($\Delta\gamma = \Gamma$). For a liquid-filled blister, considering the interfaces between the liquid, the membrane, and the substrate, the change of the interfacial energy can be written as

$$\Delta\gamma = \gamma_{ml} + \gamma_{sl} - \gamma_{ms}, \qquad [2]$$

where γ_{ml}, γ_{sl}, and γ_{ms} are the energy densities (per unit area) for the membrane–liquid interface, substrate–liquid interface, and the membrane–substrate interface, respectively. For blisters filled with liquid water, the Young–Dupré equations (37, 38) further lead to

$$\Delta\gamma = \Gamma - \gamma_w(\cos\theta_s + \cos\theta_m). \qquad [3]$$

In Eq. **3**, Γ is the work of adhesion (or adhesion energy) of the membrane–substrate interface, γ_w is the surface tension of water (~0.072 J/m^2) (38, 39), and θ_s and θ_m are the water contact angles of the substrate and the membrane, respectively. Thus, the scaling analysis predicts the aspect ratio for a liquid-filled blister as

$$\frac{h}{a} = \left(\phi\frac{\Gamma - \gamma_w(\cos\theta_m + \cos\theta_s)}{E_{2D}}\right)^{1/4}, \qquad [4]$$

where the dimensionless coefficient ϕ has to be determined by a detailed analysis (*SI Appendix*, section 2).

Clearly, by Eq. **4**, the aspect ratio of a water-filled blister depends on the elastic property of the membrane, the adhesion of the membrane to the substrate, and the hydrophobicity of the membrane and the substrate. In addition, it should also depend on the shear interactions between the membrane and the substrate in the bonded region surrounding the blister. In previous studies of graphene blisters (8, 23, 25, 29), the edge of the blister is often assumed to be fully clamped onto the substrate due to adhesion and strong shear interactions that prevent sliding along the interface. However, a recent study (31) found that the shear interactions can be fairly weak between graphene and its substrate so that sliding may occur at the edge of the blister. As a result, the elastic deformation of the membrane depends on the shear interactions with the substrate, which means the coefficient in Eq. **4** depends on the shear interactions as well. By a simple membrane analysis (*SI Appendix*, section 2), we found that $\phi = 24(1-\nu)/5(7-\nu)$ for the limiting case with no sliding at the edge, that is, the strong shear limit for the membrane–substrate interface; ν is the Poisson's ratio of the membrane material. Alternatively, $\phi = 6/5$ is predicted for the weak shear limit when the membrane–substrate interface is essentially frictionless. In this case, the elastic energy in the membrane is reduced by sliding. Compared with the strong shear limit, the weak shear limit predicts a larger aspect ratio for the blister, about 20% higher for graphene ($\nu = 0.165$) in particular.

To further examine the effect of a finite interfacial shear stress on the aspect ratio of the blisters, we performed a more rigorous analysis for the liquid-filled blisters following Hencky's approach (31, 40). Assuming a finite interfacial shear stress (τ) between the membrane and the substrate, an annular sliding zone ($a < r < \rho a$) develops outside the edge of a circular blister where ρ is a dimensionless coefficient. The blister radius (a) and the extent of the sliding zone (ρa) are both determined by minimizing the total free energy under the condition of a constant liquid volume. For a given liquid volume (V), we define a length scale as $L_w = V^{1/3}$. The normalized blister radius ($\bar{a} = a/L_w$) can be obtained as a function of three dimensionless parameters: $\bar{\tau} = \tau L_w/E_{2D}$, $\Delta\gamma/E_{2D}$, and ν. The aspect ratio (h/a) can also be derived (*SI Appendix*, Eq. **S30**). It is found that, for a membrane–substrate interface with $\bar{\tau} > 0.1$ or $\bar{\tau} < 10^{-4}$, the aspect ratio of the blister agrees closely with the predictions by Eq. **4** for the strong shear or the weak shear limit, respectively, especially under small deflection (*SI Appendix*, Fig. S8). In reality, for most 2D membranes, including graphene on SiO_2, the interfacial shear stress is fairly small as summarized in *SI Appendix*, Table S1. The weak shear limit can be used as a good approximation as long as the liquid volume in the blister or the aspect ratio is relatively small ($a < 300$ nm or $h/a < 0.1$). Moreover, considering the finite lateral size of the membrane (*SI Appendix*, Fig. S9), the Hencky's analysis is slightly modified to account for the boundary conditions (more details in *SI Appendix*, section 2), with which we find that the finite

size effect is typically negligible as long as the blister is not located close to the edge of a membrane (allowing $\rho > 4$).

MD Simulations. As a verification for our analytical model, MD simulations were conducted to simulate water-filled blisters trapped between a monolayer graphene membrane and a rigid substrate (see *SI Appendix*, section 3 for details). As predicted by Eq. **4**, the aspect ratio of the blister depends on the graphene-to-substrate adhesion energy (Γ) and the two water contact angles (θ_s and θ_m). For the MD simulations, we set θ_m to be 60° and θ_s to be 40° by selecting proper parameters for the interaction potentials between water and graphene and between water and the substrate. The interaction parameters between graphene and the substrate are varied to simulate graphene blisters with different aspect ratios as a result of different adhesion energy Γ. It is noted that it may not be possible to fully capture the mechanics, wetting, and surface chemistry by using the empirical force fields in the present study. Fig. 3 plots the MD results in comparison with the analytical predictions, along with three snapshots for the trapped water molecules ($n = 2{,}700$). When the adhesion energy is relatively large ($\Gamma > 0.2$ J/m^2), the water molecules take the shape of a spherical cap as assumed in the continuum model. In this case, the aspect ratio h/a increases with increasing adhesion energy, in close agreement with the analytical prediction assuming a frictionless interface. As expected, the results are bounded by the strong shear limit $[\phi = 24(1-\nu)/5(7-\nu)]$ and the weak shear limit ($\phi = 6/5$) for an infinitely large membrane. The weak shear limit overestimates the aspect ratio in MD due to the periodic boundary conditions employed in the MD simulations, and the strong shear limit underestimates the aspect ratio due to the assumption of no sliding. Interestingly, for the case of a lower adhesion energy ($\Gamma < 0.2$ J/m^2), the top of the blister is nearly flat, and the water molecules form a distinct bilayer structure instead of a spherical cap. As a result, the continuum assumption breaks down, and the aspect ratio becomes nearly independent of the adhesion energy for the same number of water molecules ($n = 2{,}700$). It is found that the breakdown of the continuum model depends on the adhesion energy (Γ) and the number of water molecules (n). As shown in *SI Appendix*, Fig. S13, for $\Gamma = 0.242$ J/m^2 the continuum model remains applicable for $n > 1{,}600$. However, for $\Gamma = 0.1$ J/m^2, our MD simulations predict a bilayer water structure for n up to 4,500. Hence, for $n < 4{,}500$ as limited by the computational cost of MD simulations, we could not simulate a graphene blister in the continuum regime for $\Gamma = 0.1$ J/m^2. Nevertheless, the analytical prediction based on the continuum model is confirmed by the MD simulations for the cases when the adhesion energy and the number of water molecules combine to yield a blister in the shape of a spherical cap, such as $\Gamma > 0.2$ J/m^2 and $n = 2{,}700$ in Fig. 3.

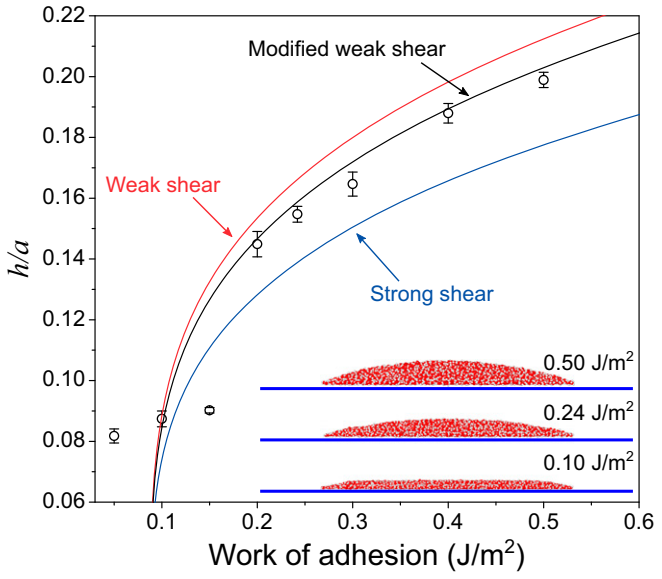

Fig. 3. Modeling and MD simulations of water-filled blisters. MD simulation results (circular markers) best agree with our simplified model assuming a frictionless, sliding interface (modified weak shear). The deviations, especially under small height or aspect ratio, are attributed to the size limitation of MD, which can induce discrete behaviors. (*Inset*) The figure demonstrates how the shape of the blister changes for different values of the work of adhesion.

Discussion and Conclusions

Having verified our theoretical analysis with MD simulations, we now apply the model to experimentally measured aspect ratio data to extract the adhesion energy for a variety of 2D material interfaces, as well as elaborate on the implications of the data for 2D material systems.

Adhesion Energy for 2D Material Interfaces. The family of 2D materials has grown appreciably in recent years (1, 2). The emergence of each new material brings demands for exploring its vdW interactions with various types of substrates and 2D materials, as many exciting applications of these materials come from stacking them into multilayers and heterostructures. Because of the significance of vdW interactions, many experimental studies have been carried out to measure the adhesion energy of 2D material interfaces, e.g., pressurized blister (8), buckling-based metrology (41–43), and double-cantilever method (44, 45), as summarized in recent review papers (3, 46). However, it is tedious or impossible to determine the adhesion energy for every pair of 2D material interfaces. Based on the present work, we propose that adhesion energy of a 2D material interface can be readily estimated by measuring the aspect ratio of spontaneously formed nanoblisters (if present). To calculate the adhesion energy, Eq. **4** is rewritten as

$$\Gamma = \frac{E_{2D}h^4}{\phi a^4} + \gamma_w(\cos\theta_m + \cos\theta_s), \qquad [5]$$

which suggests that once the relevant material properties are available, the adhesion energy can be determined by just measuring the aspect ratio of a blister. We take $\phi = 1.2$ by the weak interface model due to the typically weak interfacial shear resistance for most of 2D material interfaces (*SI Appendix*, Table S1). Note that the strong interface model gives a smaller prefactor ($\phi = 0.6$), thus overestimating the adhesion energy. Assuming water is trapped in the blisters, in Fig. 4, we calculated the graphene–SiO_2, MoS_2–SiO_2, and MoS_2–Al_2O_3 work of adhesion by using our measurements in Fig. 1. Our values are in reasonable agreement with values determined in similar systems via alternative methods (0.1–0.4 J/m^2 for graphene–SiO_2 and 0.04 J/m^2 for MoS_2–SiO_2) (32, 47, 48). We attribute our slightly lower adhesion values to: (*i*) previously neglected, but significant, interfacial sliding; (*ii*) the slight amount of contaminants which can influence the surface tension and contact angle terms for water in Eq. **3**; and (*iii*) the rough substrate surface (197 ± 19 pm in our sample) which is believed to cause scattering in adhesion measurements with SiO_2 (8). For our Al_2O_3 substrate, the surface roughness was measured to be 251 ± 10 pm. Notably, nanoblisters found in our samples often exhibit some degree of ellipticity (*SI Appendix*, Fig. S2). Therefore, only approximately circular blisters with minor-to-major axis ratios larger than 0.85 are used for the adhesion energy calculations. The resulting uncertainty in adhesion energy is calculated to be at most 1, 1, and 5 mJ/m^2

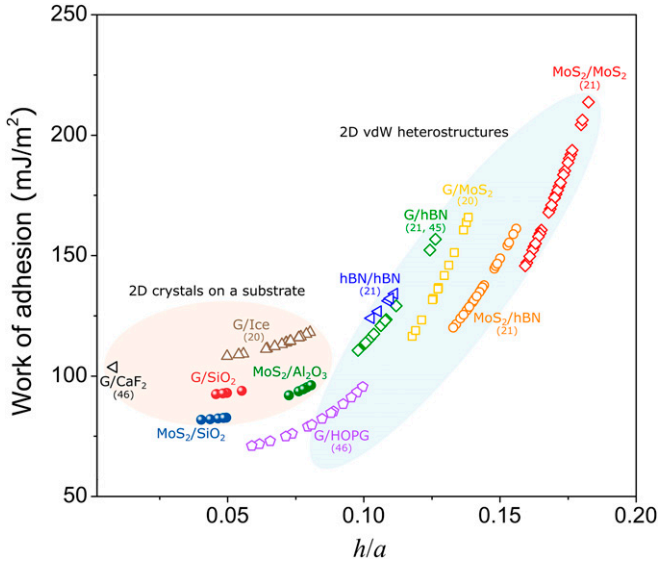

Fig. 4. Work of adhesion values for various 2D material interfaces estimated according to blister profiles, including many interfaces found in 2D heterostructures. Solid markers indicate our own experiments while open markers are for blisters reported in the literature.

for graphene–SiO_2, MoS_2–SiO_2, and MoS_2–Al_2O_3 interfaces, respectively.

We further provide a survey of the relevant parameters from several studies of water-filled blisters in the literature (13, 20, 49). The material properties used in adhesion energy calculations are summarized in *SI Appendix*, section 4. By substituting these values into Eq. **5**, we are able to estimate the interfacial adhesion energies for a variety of interfaces (Fig. 4, also summarized in Table 1). If the affinity between the 2D crystal and its substrate is smaller than the affinity of the 2D crystal to the entrapped liquid, then the energetically favorable configuration should be the one that maximizes the contact between the 2D crystal and the liquid. To achieve this configuration, the liquid would spread out and form a layered, ice-like structure with almost zero h/a. Our model can hence predict an upper limit for the adhesion energy of these 2D material interfaces as $\Gamma \leq \gamma_w(\cos\theta_m + \cos\theta_s)$ (noted as the yellow region in Table 1). This simple relation also quantitatively offers a criterion for the interesting observation of room-temperature ice formation in a 2D nanochannel (50–56). This formula can also help explain the so-called self-cleaning mechanism (formation of blisters) which is typically observed at atomically smooth, hydrophobic 2D heterostructure interfaces such as graphene–V_2O_5 (9).

Knowing the adhesion values of various vdW interfaces of 2D crystals is very beneficial to the fabrication of 2D crystal-based devices. The fabrication typically involves either exfoliation of 2D layers from bulk crystal or transfer of synthesized 2D crystals from a donor substrate to a target substrate. Such processes rely on the competing adhesion energies between the 2D crystal and its "stamp," and the various surfaces that it contacts. For example, Brennan et al. (43) reported the adhesion of MoS_2 to polydimethylsiloxane is 18 ± 2 mJ/m^2, which is relatively weak compared with the adhesion between MoS_2 and SiO_2, or MoS_2 and graphene, as estimated in Fig. 4. As a result, delivering 2D MoS_2 to those substrates from an elastomeric stamp is mechanically viable (57–60). Therefore, the adhesion energy values obtained by our blister metrology (Fig. 4) can help guide and optimize the transfer of 2D materials.

Implications for Applications of 2D Material Blisters. We conclude by highlighting some of the implications of our work for the applications of 2D material blisters. In addition to adhesion energy, our liquid-filled blister model can also predict the confinement pressure, Δp, inside the blisters and the strain distribution in the 2D membrane. The confinement pressure was previously estimated by capturing pressure-sensitive molecules trapped inside the blister, studying molecular structural and conformational changes, and observing the specific chemistry inside the blister (17, 19). Our model offers a direct relation between the confinement pressure and the geometry of the blisters (*SI Appendix*, section 2), namely

$$\Delta p = \frac{1}{a}\left(\eta E_{2D}\frac{h^3}{a^3}\right), \qquad [6]$$

where $\eta \simeq 3.1$ for a graphene blister with a strong shear interface and $\eta \simeq 1.6$ for a weak shear interface. Note that unlike the adhesion energy, which only depends on the aspect ratio of the blister, the confinement pressure given in Eq. **6** depends on the size of the blister and has to be estimated with both the height and radius known. For a particular 2D material and interface, the aspect ratio (h/a) is a constant and the confining pressure is inversely proportional to the blister radius. For the water-filled nanoblisters confined between MoS_2 and Al_2O_3 in our experiment (e.g., h = 4 nm, a = 50 nm), we estimate the confinement pressure to be around 7 MPa. Note that the strain distribution in the blisters can also be estimated based on our analysis (Eqs. **S4** and **S5** in *SI Appendix*, section 2).

Furthermore, in applications of 2D material blisters it is vital that the blister shape and confinement conditions can be controlled. Eq. **3** provides a direct guidance to the aspect ratio of the blisters. For a given interface with fixed adhesion, trapping different types of liquids with different surface energies and contact angles can tune the blister shape and membrane strain. In fact, a recent study by Neek-Amal and coworkers (12) demostrated the dependence of the shape of graphene nanoblisters on trapped substance. Our proposed strategies are also consistent with our MD simulations in Fig. 3.

Materials and Methods

The monolayer graphene and MoS_2 samples were mechanically exfoliated from their respective bulk crystals onto a 300-nm SiO_2/Si substrate. The

Table 1. Estimation of adhesion energy via blister profiles

Interface type	Materials (ref)	Adhesion energy (mJ/m^2)
2D crystal vdW heterostructures	MoS_2–MoS_2 (13)	174 ± 18
	G–MoS_2 (20)	140 ± 26
	MoS_2–hBN (13)	136 ± 11
	hBN–hBN (13)	129 ± 4
	G–hBN (13, 49)	126 ± 20
	G–HOPG (22)	86 ± 16
2D crystal on a substrate	G-Ice (20)	124 ± 30
	G–CaF_2 (28)	104
	MoS_2–Al_2O_3*	101 ± 15
	G–SiO_2*	93 ± 1
	MoS_2–SiO_2*	82 ± 1
Graphene interfaces without blisters	G–V_2O_5 (9)	≤108
	G–sapphire (50)	≤107
	G–Mica (51–54)	≤102
	G–Si (55)	≤72
	G–SiC (56)	≤57

*Data from Fig. 1*D*; Other data are from water-filled 2D materials blisters except data from ref. 13, which suggested hydrocarbon and water blister contents.

MoS_2–Al_2O_3 sample fabrication and characterization details are in a previous work (60). Further detail is provided in *SI Appendix*, section 1.

ACKNOWLEDGMENTS. Z.D. acknowledges the Warren A. and Alice L. Meyer Endowed Scholarship in Engineering. N.L. and D.A.S. thank Prof. Xiaoqin Li and Mr. Kha Tran [The University of Texas at Austin (UT Austin)] for the discussions about exfoliating and transferring 2D materials. D.A.S. acknowledges Dr. Raluca Gearba and Dr. Andrei Dolocan (UT Austin) for their assistance in using the Texas Material Institute facilities. This work is supported by the NSF Division of Civil, Mechanical and Manufacturing Innovation (CMMI) under Grants 1351875 and 1562820. D.A.S. acknowledges support from the NSF Graduate Research Fellowship Program; the Graduate Education for Minorities Fellowship; the T. W. Whaley, Jr. Friends of Alec Endowed Scholarship of the NSF Nanosystems Engineering Research Center (NERC) for Nanomanufacturing Systems for Mobile Computing and Mobile Energy Technologies (NASCENT); and the Virginia and Ernest Cockrell, Jr. Fellowship of UT Austin.

1. Novoselov KS, Mishchenko A, Carvalho A, Castro Neto AH (2016) 2D materials and van der Waals heterostructures. *Science* 353:aac9439.
2. Geim AK, Grigorieva IV (2013) Van der Waals heterostructures. *Nature* 499:419–425.
3. Akinwande D, et al. (2017) A review on mechanics and mechanical properties of 2D materials—Graphene and beyond. *Extreme Mech Lett* 13:42–77.
4. Klimov NN, et al. (2012) Electromechanical properties of graphene drumheads. *Science* 336:1557–1561.
5. Levy N, et al. (2010) Strain-induced pseudo-magnetic fields greater than 300 tesla in graphene nanobubbles. *Science* 329:544–547.
6. Koren E, Lörtscher E, Rawlings C, Knoll AW, Duerig U (2015) Surface science. Adhesion and friction in mesoscopic graphite contacts. *Science* 348:679–683.
7. Kitt AL, et al. (2013) How graphene slides: Measurement and theory of strain-dependent frictional forces between graphene and SiO2. *Nano Lett* 13:2605–2610.
8. Koenig SP, Boddeti NG, Dunn ML, Bunch JS (2011) Ultrastrong adhesion of graphene membranes. *Nat Nanotechnol* 6:543–546.
9. Kretinin AV, et al. (2014) Electronic properties of graphene encapsulated with different two-dimensional atomic crystals. *Nano Lett* 14:3270–3276.
10. Pizzocchero F, et al. (2016) The hot pick-up technique for batch assembly of van der Waals heterostructures. *Nat Commun* 7:11894.
11. Lloyd D, et al. (2016) Band gap engineering with ultralarge biaxial strains in suspended monolayer MoS2. *Nano Lett* 16:5836–5841.
12. Ghorbanfekr-Kalashami H, Vasu KS, Nair RR, Peeters FM, Neek-Amal M (2017) Dependence of the shape of graphene nanobubbles on trapped substance. *Nat Commun* 8:15844.
13. Khestanova E, Guinea F, Fumagalli L, Geim AK, Grigorieva IV (2016) Universal shape and pressure inside bubbles appearing in van der Waals heterostructures. *Nat Commun* 7:12587.
14. Chen Z, et al. (2017) Interface confined hydrogen evolution reaction in zero valent metal nanoparticles-intercalated molybdenum disulfide. *Nat Commun* 8:14548.
15. Lim CHYX, et al. (2013) A hydrothermal anvil made of graphene nanobubbles on diamond. *Nat Commun* 4:1556.
16. Lu J, Neto AH, Loh KP (2012) Transforming Moiré blisters into geometric graphene nano-bubbles. *Nat Commun* 3:823.
17. Vasu KS, et al. (2016) Van der Waals pressure and its effect on trapped interlayer molecules. *Nat Commun* 7:12168.
18. Zamborlini G, et al. (2015) Nanobubbles at GPa pressure under graphene. *Nano Lett* 15:6162–6169.
19. Lim CHYX, Nesladek M, Loh KP (2014) Observing high-pressure chemistry in graphene bubbles. *Angew Chem Int Ed Engl* 53:215–219.
20. Bampoulis P, Teernstra VJ, Lohse D, Zandvliet HJ, Poelsema B (2016) Hydrophobic ice confined between graphene and MoS2. *J Phys Chem C* 120:27079–27084.
21. Haigh SJ, et al. (2012) Cross-sectional imaging of individual layers and buried interfaces of graphene-based heterostructures and superlattices. *Nat Mater* 11:764–767.
22. Cao P, Xu K, Varghese JO, Heath JR (2011) The microscopic structure of adsorbed water on hydrophobic surfaces under ambient conditions. *Nano Lett* 11:5581–5586.
23. Yue K, Gao W, Huang R, Liechti KM (2012) Analytical methods for the mechanics of graphene blisters. *J Appl Phys* 112:083512.
24. An H, et al. (2017) Graphene nanobubbles produced by water splitting. *Nano Lett* 17:2833–2838.
25. Falin A, et al. (2017) Mechanical properties of atomically thin boron nitride and the role of interlayer interactions. *Nat Commun* 8:15815.
26. Huang Y, et al. (2015) Reliable exfoliation of large-area high-quality flakes of graphene and other two-dimensional materials. *ACS Nano* 9:10612–10620.
27. Ferrari AC, et al. (2006) Raman spectrum of graphene and graphene layers. *Phys Rev Lett* 97:187401.
28. Temmen M, Ochedowski O, Schleberger M, Reichling M, Bollmann T (2014) Hydration layers trapped between graphene and a hydrophilic substrate. *New J Phys* 16:053039.
29. Wang P, Gao W, Cao Z, Liechti KM, Huang R (2013) Numerical analysis of circular graphene blisters. *J Appl Mech* 80:040905.
30. Drahushuk LW, Wang L, Koenig SP, Bunch JS, Strano MS (2016) Analysis of time-varying, stochastic gas transport through graphene membranes. *ACS Nano* 10:786–795.
31. Wang G, et al. (2017) Measuring interlayer shear stress in bilayer graphene. *Phys Rev Lett* 119:036101.
32. Boddeti NG, et al. (2013) Graphene blisters with switchable shapes controlled by pressure and adhesion. *Nano Lett* 13:6216–6221.
33. Berry V (2013) Impermeability of graphene and its applications. *Carbon* 62:1–10.
34. Ahmadpoor F, Wang P, Huang R, Sharma P (2017) Thermal fluctuations and effective bending stiffness of elastic thin sheets and graphene: A nonlinear analysis. *J Mech Phys Solids* 107:294–319.
35. Gao W, Huang R (2014) Thermomechanics of monolayer graphene: Rippling, thermal expansion and elasticity. *J Mech Phys Solids* 66:42–58.
36. Lee C, Wei X, Kysar JW, Hone J (2008) Measurement of the elastic properties and intrinsic strength of monolayer graphene. *Science* 321:385–388.
37. Israelachvili J (1991) *Intermolecular and Surface Forces* (Academic, London), 2nd Ed.
38. Rafiee J, et al. (2012) Wetting transparency of graphene. *Nat Mater* 11:217–222.
39. Seemann R, Herminghaus S, Jacobs K (2001) Dewetting patterns and molecular forces: A reconciliation. *Phys Rev Lett* 86:5534–5537.
40. Fichter WB (1997) Some solutions for the large deflections of uniformly loaded circular membranes (National Aeronautics and Space Administration, Langley Research Center, Hampton, VA), NASA Technical Paper 3658.
41. Jiang T, Huang R, Zhu Y (2013) Interfacial sliding and buckling of monolayer graphene on a stretchable substrate. *Adv Funct Mater* 24:396–402.
42. Dai Z, et al. (2016) Mechanical behavior and properties of hydrogen bonded graphene/polymer nano-interfaces. *Compos Sci Technol* 136:1–9.
43. Brennan CJ, Nguyen J, Yu ET, Lu N (2015) Interface adhesion between 2D materials and elastomers measured by buckle delaminations. *Adv Mater Interfaces* 2:1500176.
44. Yoon T, et al. (2012) Direct measurement of adhesion energy of monolayer graphene as-grown on copper and its application to renewable transfer process. *Nano Lett* 12:1448–1452.
45. Na SR, Suk JW, Ruoff RS, Huang R, Liechti KM (2014) Ultra long-range interactions between large area graphene and silicon. *ACS Nano* 8:11234–11242.
46. Bunch JS, Dunn ML (2012) Adhesion mechanics of graphene membranes. *Solid State Commun* 152:1359–1364.
47. Lloyd D, et al. (2017) Adhesion, stiffness, and instability in atomically thin MoS_2 bubbles. *Nano Lett* 17:5329–5334.
48. Zong Z, Chen C-L, Dokmeci MR, Wan K-t (2010) Direct measurement of graphene adhesion on silicon surface by intercalation of nanoparticles. *J Appl Phys* 107:026104.
49. Uwanno T, Hattori Y, Taniguchi T, Watanabe K, Nagashio K (2015) Fully dry PMMA transfer of graphene on h-BN using a heating/cooling system. *2D Mater* 2:041002.
50. Komurasaki H, Tsukamoto T, Yamazaki K, Ogino T (2012) Layered structures of interfacial water and their effects on Raman spectra in graphene-on-sapphire systems. *J Phys Chem C* 116:10084–10089.
51. He KT, Wood JD, Doidge GP, Pop E, Lyding JW (2012) Scanning tunneling microscopy study and nanomanipulation of graphene-coated water on mica. *Nano Lett* 12:2665–2672.
52. Shim J, et al. (2012) Water-gated charge doping of graphene induced by mica substrates. *Nano Lett* 12:648–654.
53. Ochedowski O, Bussmann BK, Schleberger M (2014) Graphene on mica–Intercalated water trapped for life. *Sci Rep* 4:6003.
54. Xu K, Cao P, Heath JR (2010) Graphene visualizes the first water adlayers on mica at ambient conditions. *Science* 329:1188–1191.
55. Gowthami T, Tamilselvi G, Jacob G, Raina G (2015) The role of ambient ice-like water adlayers formed at the interfaces of graphene on hydrophobic and hydrophilic substrates probed using scanning probe microscopy. *Phys Chem Chem Phys* 17:13964–13972.
56. Kazakova O, Panchal V, Burnett TL (2013) Epitaxial graphene and graphene–based devices studied by electrical scanning probe microscopy. *Crystals (Basel)* 3:191–233.
57. Wang G, et al. (2015) Biaxial compressive behavior of embedded monolayer graphene inside flexible poly (methyl methacrylate) matrix. *Carbon* 86:69–77.
58. Wang G, et al. (2016) Tuning the interfacial mechanical behaviors of monolayer graphene/PMMA nanocomposites. *ACS Appl Mater Interfaces* 8:22554–22562.
59. Wang G, et al. (2017) Degradation and recovery of graphene/polymer interfaces under cyclic mechanical loading. *Compos Sci Technol* 149:220–227.
60. Brennan CJ, et al. (2017) Out-of-plane electromechanical response of monolayer molybdenum disulfide measured by piezoresponse force microscopy. *Nano Lett* 17:5464–5471.

Supporting Appendix

Mechanics of Spontaneously Formed Nanoblisters Trapped by Transferred 2D Crystals

Daniel A. Sanchez[a, 1], Zhaohe Dai[b, 1], Peng Wang[b], Arturo Cantu-Chavez[a], Christopher J. Brennan[c], Rui Huang[a, b, 2], Nanshu Lu[a, b, c, d, 2]

[a] *Texas Materials Institute, The University of Texas at Austin, Austin, Texas 78712, USA.*

[b] *Center for Mechanics of Solids, Structures and Materials, Department of Aerospace Engineering and Engineering Mechanics, The University of Texas at Austin, Austin, Texas 78712, USA.*

[c] *Department of Electrical and Computer Engineering, The University of Texas at Austin, Austin, Texas, 78712, USA.*

[d] *Department of Biomedical Engineering, The University of Texas at Austin, Austin, Texas, 78712, USA.*

[1] These authors contributed equally to this work.

[2] To whom correspondence may be addressed. E-mail: Nanshu Lu (nanshulu@utexas.edu), Rui Huang (ruihuang@mail.utexas.edu)

The purpose of this supporting information is to provide detailed experimental data, derivation of the equations discussed in the manuscript, details of molecular dynamics (MD) simulations, and materials properties we adopted. In Section 1 we present the nanoblisters observed in MoS_2 samples, the Raman evidence for the monolayer graphene and MoS_2, and our analysis of blister ellipticity. In Section 2 we describe the approximate membrane analysis and solve Hencky's problem for comparison. In Section 3 we present detailed MD simulations for water blisters trapped between a monolayer graphene and a rigid substrate. In Section 4 we summarize the moduli, water contact angles, interfacial shear/friction properties of various 2D materials and substrate materials, by which we created the adhesion chart (Fig. 4) in the manuscript.

www.pnas.org/cgi/doi/10.1073/pnas.1801551115

Section 1: Experimental methods and analysis.

Sample preparation and characterization. SPI-1 grade HOPG was purchased from SPI Supplies, and the synthetic MoS_2 crystal was purchased from 2D Semiconductors, Inc. The same exfoliation procedure is used for both crystals. Blue polyethylene cleanroom tape (CRT) was used to peel large and thick flake off the bulk crystal. The exfoliated flakes were then brought into contact with another piece of the CRT and exfoliated three more times. The flakes were then stored for a minimum of 3 hours in ambient conditions to allow ambient moisture and other contents to adsorb on the surface of the exposed flakes. The 300 nm SiO_2/Si substrate wafer (SQI Inc., Item No. 20040830) was first prepared by cutting a 1 cm × 1 cm chip from the wafer. The chip was then washed with acetone, isopropyl alcohol, and deionized water, while sonicating for 3 minutes during each step. To maximize the area of monolayer regions that were transferred to SiO_2 (33), the SiO_2 chip was exposed to O_2 plasma using a Nordson MARCH Plasma CS170IF Etching System for 2 minutes at 150 W to remove any organic residue. Immediately after O_2 plasma exposure, the exfoliated HOPG flakes on CRT were placed onto the surface of the SiO_2 chip. Then the SiO_2 chip was placed on a hot plate and was heated at 100°C for two minutes. The sample was removed from the hot plate and cooled to room temperature, after which the CRT was removed. Topographic AFM images for graphene-SiO_2, MoS_2-SiO_2 and MoS_2-Al_2O_3 samples are offered in Fig. 1B, Fig. S1A, and Fig. S1B, respectively. Monolayer regions on the SiO_2 chip were identified using a WITec alpha300 Raman spectrometer using a laser wavelength of 532 nm. In Fig. 1A, the three areas where Raman measurements were taken is marked with colored dots. Fig. S1C shows the Raman spectra for each region. The 2D/G peak ratio was 3.9 for regions 1 and 3 and 3.1 for region 2, which indicates that all three regions are monolayer graphene (1). For the MoS_2 on SiO_2 sample (Fig. S1D), the E^1_{2g} and A_{1g} modes were located at 385.4 cm^{-1} and 404.1 cm^{-1}, respectively. The wavenumber difference between the modes, 18.7 cm^{-1}, is indicative of the monolayer thickness of the flake (2).

The MoS_2 on Al_2O_3 sample in this work is at a different location on the same sample as used in a previous work, where the fabrication and characterization details can be found (3). Briefly, CVD-grown MoS_2 was transferred onto ALD-grown, 5.3 nm thick Al_2O_3 using a polydimethylsiloxane (PDMS) stamp.

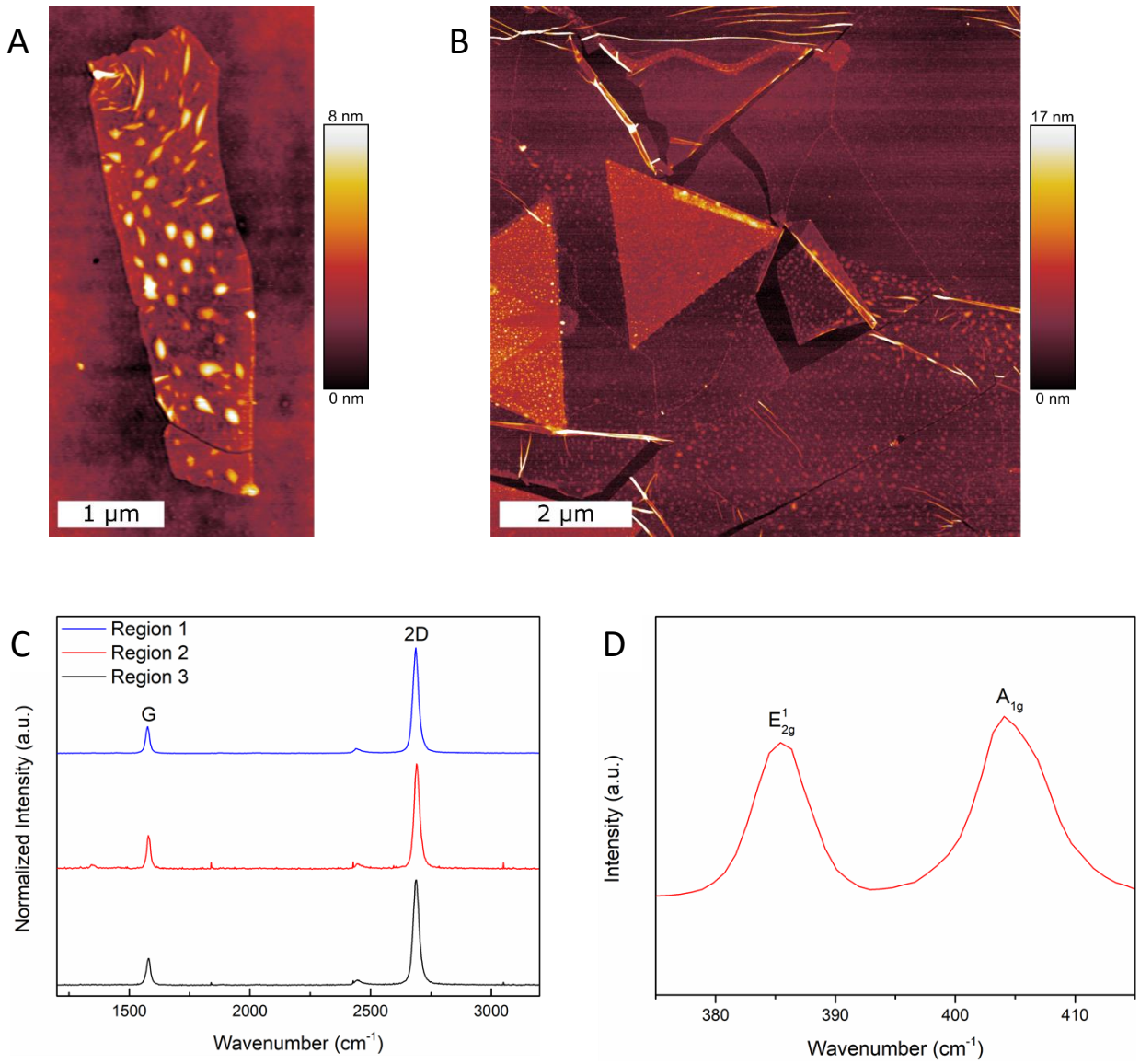

Figure S1. Characterization of MoS_2 blisters. Topographic AFM images for the (*A*) MoS_2-SiO_2 and (*B*) MoS_2-Al_2O_3 samples. (*C*) Raman spectroscopy for all SLG regions, and (*D*) for the monolayer MoS_2 on SiO_2 flake.

Analysis of graphene-SiO_2 blister distributions. Interestingly, the blisters tend to have a periodic distribution throughout the graphene-SiO_2 interface. Fig. S2A and S2B show the distributions of the blister pitch measured as the center-to-center distance between adjacent blisters. The average pitch for single-layer graphene (SLG) is 1548 ± 430 nm, while the average pitch for few-layer graphene (FLG) is 1661 ± 354 nm.

Another interesting characteristic of the graphene-SiO_2 blisters in Fig. 1A lies in their varying degrees of ellipticity. Elliptical blisters were noted in the main text and speculated to form

as a result of the blister's proximity to the graphene boundary. To characterize this phenomenon, we define the blister ellipticity as the ratio $\alpha = a_s/a_l$, where a_s and a_l are the radii along the semi-minor and semi-major ellipse axes, respectively. Additionally, we define $\rho = d/a_s$, where d is the shortest distance from the center of the blister to the graphene boundary. The two dimensionless parameters are plotted in Fig. S2C. Linear regression analysis does not provide an adequate description of the relationship between ρ and α ($R^2 = 0.42$), but the overall trend supports our conclusion that circular blisters are more likely to be found far away from graphene boundaries. Close to the boundary, elliptical blisters tend to form with the major axis parallel to the boundary. Since circular blisters with $\alpha = 1$ are rarely found, we adopted a cutoff criterion for a blister with $\alpha \geq 0.85$ in order to be considered as approximately circular so that it is eligible for the adhesion energy calculation.

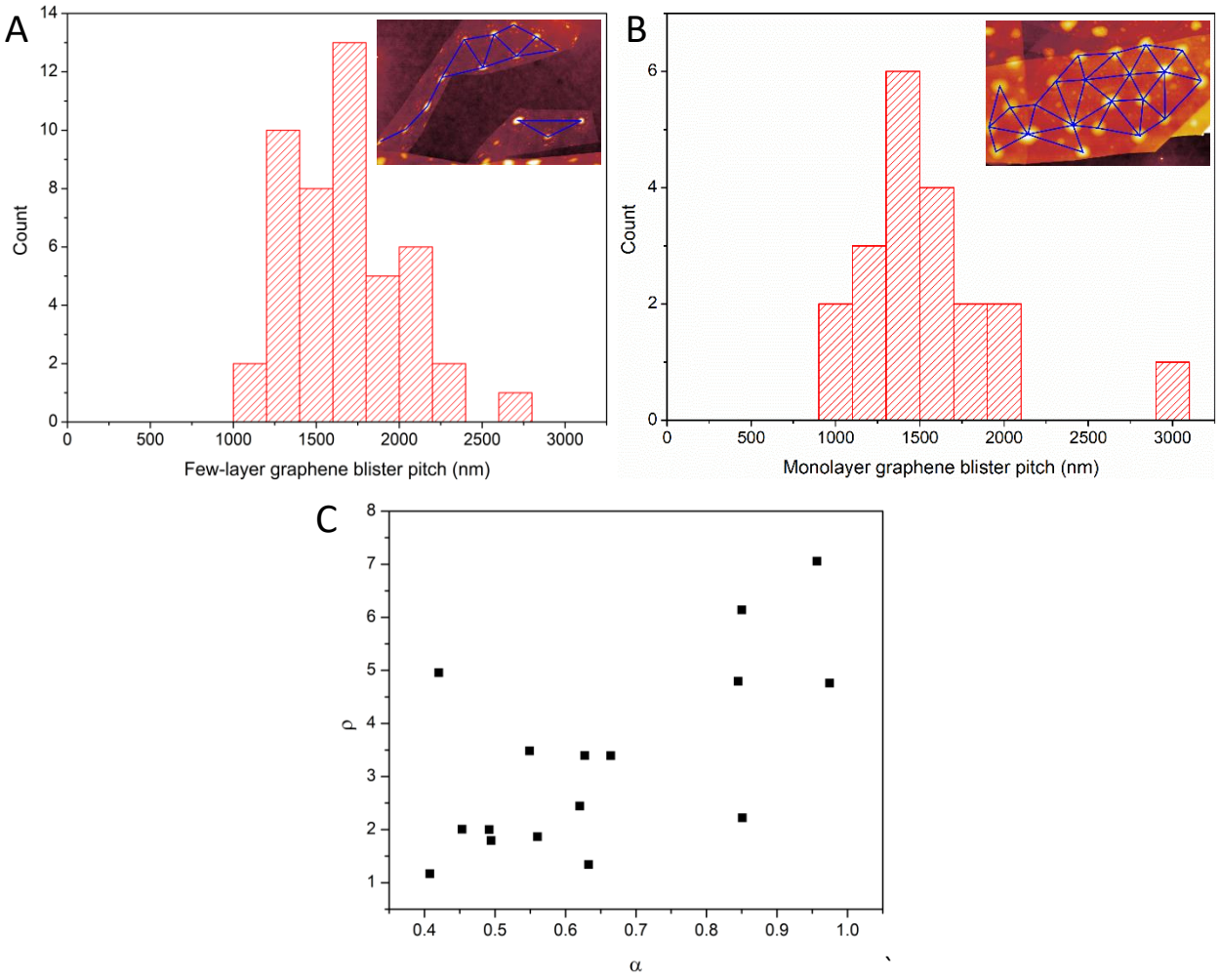

Figure S2. Analysis of blister pitch distributions and ellipticity. Histogram pitch distributions for (*A*) SLG-SiO_2 and (*B*) FLG-SiO_2. The inset for both figures demonstrates how the pitch is calculated. (*C*) Dimensionless distance from graphene edge to blister center as a function of the blister ellipticity ratio.

Blister profile measurements. The AFM topography images for graphene-SiO_2 and MoS_2-SiO_2 blisters were captured using an Asylum Research MFP3D AFM in tapping mode with MikroMasch HQ:NSC15/Al BS cantilever tips under ambient conditions. The topography image for MoS_2-Al_2O_3 was captured using a Bruker (formerly Veeco) Dimension Icon AFM using etched silicon cantilevers (Bruker TESP). AFM image files were processed using Gwyddion software. The height profile of each blister was extracted from the AFM height sensor image by identifying the tallest point of each blister; then the height profile of the blister was measured through this point along a vertical line relative to the AFM image for all blisters for consistency. For adhesion energy calculations, a second-order polynomial of the form $w(r) = C_1 r^2 + C_2 r + C_3$ was fitted to the blister height profile using Excel. Given the form of the blister deflection profile (Eq. **1** in main text), h and a were obtained as $h = C_3$ and $a = -\left(\frac{h}{C_1}\right)^{1/2}$ after centering the blister profile about the $r = 0$ axisymmetric axis.

In the time-lapse calculations, the height profile of the blisters became less parabolic after the initial AFM scan thus requiring the calculations of h and a using a more general method. For the height measurement, $h = h^{max} - \frac{h_{left}^{min} - h_{right}^{min}}{2}$, where h^{max} is the maximum vertical height, and h_{left}^{min} and h_{right}^{min} are the minimum height values on either side of the blister profile. For the radius measurement, $a = \frac{a_{left}^{min} - a_{right}^{min}}{2}$, where a_{left}^{min} and a_{right}^{min} are the horizontal positions of h_{left}^{min} and h_{right}^{min}, respectively.

Section 2: Analytical modelling of liquid-filled nanoblisters.

By a scaling analysis as presented in the main text, the height-to-radius aspect ratio of a liquid-filled nanoblister is predicted as:

$$\frac{h}{a} = \left(\phi \frac{\Gamma - \gamma_w(\cos\theta_m + \cos\theta_s)}{E_{2D}}\right)^{\frac{1}{4}}, \quad (1)$$

where the dimensionless coefficient ϕ has to be determined by a detailed analysis. Previous studies on graphene gas blisters (4) predicted a similar scaling (but with $\gamma_w = 0$) by assuming the ideal

gas law for the pressure inside the blister, where the coefficient ϕ was found to be a function of Poisson's ratio of the membrane material. The edge of the blister is often assumed to be fully clamped onto the substrate due to adhesion and strong shear interactions that prevent sliding along the interface. However, a recent study (5) found that the shear interactions can be fairly weak between graphene and its substrate so that sliding may occur at the edge of the blister. As a result, the elastic deformation of the membrane depends on the shear interactions, and, in turn, the coefficient ϕ depends on the shear interactions as well. Here, we first consider two limiting cases by a simple membrane analysis, one for blisters with fully clamped edge (strong shear limit) and the other for blisters with frictionless sliding interface (weak shear limit). This is followed by a more rigorous analysis by Hencky's approach (6, 7), with the shear interactions represented by a finite interfacial shear stress between the membrane and the substrate. The effects of the finite membrane size and outer boundary conditions are discussed.

A simple membrane analysis for strong and weak shear limits. As in previous studies (4, 8, 9), in this simple membrane analysis, the deflection profile of the membrane for is assumed to be:

$$w(r) = h\left(1 - \frac{r^2}{a^2}\right), \tag{2}$$

where the height h is relatively small compared to the blister radius a. For a liquid-filled blister, the liquid within the blister is assumed to be incompressible so that the blister volume, $V = \pi a^2 h/2$, remains a constant. The area of the bulged surface $A' = \pi(a^2 + h^2) \approx \pi a^2$ for small h/a ratio. For a given liquid volume, the aspect ratio (h/a) of the blister is determined by the competition between the elastic strain energy of the membrane and the interfacial energy.

To calculate the elastic strain energy of the membrane, we assume a cubic radial displacement that is kinematically admissible:

$$u(r) = u_0 \frac{r}{a}\left(1 - \frac{r^2}{a^2}\right) + u_s \frac{r}{a}, \tag{3}$$

where u_0 is to be determined and u_s accounts for the in-plane sliding at the edge of the blister ($r = a$). For the strong shear limit, $u_s = 0$. For the weak shear limit, u_s is to be determined by considering elastic deformation of the membrane outside the edge of the blister. Note that the cubic radial displacement function yields a better approximation than a quadratic function used in a previous study (4), as shown recently in comparison with MD simulations (8, 9). A more accurate

solution is presented later in the SI by assuming a seven-term polynomial for the displacements, where the first two terms are linear and cubic for the radial displacement.

With Eqs. (2) and (3), the radial and circumferential strain components are obtained as:

$$\varepsilon_r = \frac{du}{dr} + \frac{1}{2}\left(\frac{dw}{dr}\right)^2 = \frac{u_s}{a} + \frac{u_0}{a}\left(1 - \frac{3r^2}{a^2}\right) + \frac{2h^2r^2}{a^4}, \tag{4}$$

$$\varepsilon_\theta = \frac{u}{r} = \frac{u_s}{a} + \frac{u_0}{a}\left(1 - \frac{r^2}{a^2}\right) \tag{5}$$

Note that the circumferential strain (ε_θ) is in general not zero at the edge ($r = a$), unless the sliding displacement u_s is zero (e.g., at the strong shear limit). We can now derive the elastic strain energy, consisting of two parts, one due to stretching and the other due to bending. The elastic stretching energy per unit area of the membrane is

$$U_s(r) = \frac{E_{2D}}{2(1-\nu^2)}({\varepsilon_r}^2 + 2\nu\varepsilon_r\varepsilon_\theta + {\varepsilon_\theta}^2), \tag{6}$$

where E_{2D} is 2D Young's modulus of the membrane material and ν is Poisson's ratio. The elastic bending energy per unit area is

$$U_b(r) = \frac{D}{2}\left[\left(\frac{d^2w}{dr^2}\right)^2 + \frac{1}{r^2}\left(\frac{dw}{dr}\right)^2 + \frac{2\nu}{r}\frac{dw}{dr}\frac{d^2w}{dr^2}\right], \tag{7}$$

where D is bending stiffness of the membrane. For graphene and other 2D membrane materials, the bending stiffness is very small so that the bending energy is negligible for typical blisters as considered in the present study.

We first consider the strong shear limit with $u_s = 0$. In this case, the membrane outside the blister edge is not deformed. The free energy for the blister is then obtained as a function of two kinematic parameters:

$$F(a, u_0) = 2\pi \int_0^a U_s(r)\, r dr + \pi a^2 \Delta\gamma, \tag{8}$$

where $\Delta\gamma = \gamma_{ml} + \gamma_{sl} - \gamma_{ms}$ is the change of interface energy for the formation of a liquid-filled blister with γ_{ml}, γ_{sl}, and γ_{ms} being the interfacial energy densities respectively for three interfaces involved: membrane-liquid interface, substrate-liquid interface, and membrane-substrate interface. For blisters filled with liquid water, the interfacial energies can be obtained from the water contact angles as $\Delta\gamma = \Gamma - \gamma_w(\cos\theta_s + \cos\theta_m)$, where Γ is adhesion energy of the membrane to the substrate, γ_w is surface tension of water, θ_s and θ_m are the water contact angles of the substrate and the membrane, respectively. We note that, unlike gas-pressurized blisters, the height of the

blister, h ($=\frac{2V}{\pi a^2}$), is not an independent variable in Eq. (8) due to the assumption of incompressible liquid with a constant volume.

For a fixed radius, the mechanical equilibrium requires that

$$\left(\frac{\partial F}{\partial u_0}\right)_a = 0, \tag{9}$$

which leads to $u_0 = \frac{(3-\nu)h^2}{4a}$. Then, with the liquid volume fixed inside the blister, the free energy is obtained as a function of the blister radius:

$$F(a) = \frac{2(7-\nu)E_{2D}V^4}{3\pi^3(1-\nu)a^{10}} + \pi a^2 \Delta\gamma. \tag{10}$$

The first term on the right-hand side of Eq. (10) is the elastic strain energy in the membrane, which decreases with increasing blister radius a. The second term stems from the change of interface energy, which increases with increasing blister radius for $\Delta\gamma > 0$. The competition of the two leads to an equilibrium blister radius that minimizes the free energy, namely

$$\left(\frac{\partial F}{\partial a}\right)_V = 0, \tag{11}$$

which gives rise to Eq. (1) with $\phi = \frac{24(1-\nu)}{5(7-\nu)}$ for the strong shear limit. Specifically, for graphene ($\nu = 0.165$), we have $\phi = 0.6$ for the strong shear limit.

Next consider the weak shear limit, where the membrane in the annular region outside of the blister edge ($r > a$) slides inward as the liquid pressure pushes up the membrane to form a blister. With zero shear stress at the frictionless interface between the membrane and the substrate, the stress and displacement in the annular region can be obtained as the classical Lamé problem in linear elasticity. The radial and circumferential components of the membrane stress are (10):

$$N_r = \frac{C_1}{r^2} + C_2, \tag{12a}$$

$$N_\theta = -\frac{C_1}{r^2} + C_2, \tag{12b}$$

where $N_r = \sigma_r t$ and $N_\theta = \sigma_\theta t$; σ_r and σ_θ are, respectively, radial and circumferential stresses; t is the membrane thickness. Correspondingly, the radial displacement is

$$u = \frac{1}{E_{2D}}\left[-\frac{(1+\nu)C_1}{r} + C_2(1-\nu)r\right]. \tag{13}$$

For an infinitely large membrane, both the stress and the displacement approach zero as $r \to \infty$, which requires $C_2 = 0$. At the edge of the blister ($r = a$), the radial stress and displacement are

continuous. By comparing Eq. (13) with Eq. (3), we obtain $C_1 = -\frac{E_{2D}au_s}{1+v}$ for the displacement continuity. For the radial stress, we have by Hooke's law

$$N_r = \frac{E_{2D}}{1-\nu^2}(\varepsilon_r + \nu\varepsilon_\theta), \tag{14}$$

where the strain components on the right-hand side are given by Eqs. (4) and (5) at $r = a$, and the radial stress on the left-hand side is given by Eq. (12a) at $r = a$. The stress continuity then leads to $u_s = u_0 - h^2/a$, where u_0 is yet to be determined for this case.

By Eq. (6) we compute the elastic stretching energy per unit area of the membrane. For the region within the blister edge ($r < a$), the strain components are given by Eqs. (4) and (5). For the annular region outside the blister edge ($r > a$), the strain components can be obtained as: $\varepsilon_r = \frac{du}{dr} = -\frac{au_s}{r^2}$ and $\varepsilon_\theta = \frac{u}{r} = \frac{au_s}{r^2}$. Then, the free energy for the blister at the weak shear limit is

$$F(a, u_0) = 2\pi \int_0^a U_S(r)\, r dr + 2\pi \int_a^\infty U_S(r)\, r dr + \pi a^2 \Delta\gamma. \tag{15}$$

Following the same process in Eq. (9), we obtain $u_0 = \frac{(3-\nu)h^2}{4a}$ and the free energy function

$$F(a) = \frac{8E_{2D}V^4}{3\pi^3 a^{10}} + \pi a^2 \Delta\gamma. \tag{16}$$

Minimization of the free energy with respect to a gives rise to Eq. (1) again, with $\phi = \frac{6}{5}$ for the weak shear limit. Compared to the strong shear limit, the weak shear limit predicts a larger height-to-radius ratio for the blister, about 20% higher for graphene in particular.

To compare with MD simulations (Section 3), where the graphene/substrate interface is frictionless and periodic boundary conditions are applied with a finite-sized graphene membrane, the analysis for the weak shear limit is modified so that the radial displacement in Eq. (13) is zero at $r = L_m$, for the square-shaped membrane with half side length of L_m in MD simulations. As a result, $C_2 = \frac{(1+\nu)C_1}{(1-\nu)L_m^2}$ and $u = \frac{(1+\nu)C_1}{E_{2D}L_m}\left[-\frac{L_m}{r} + \frac{r}{L_m}\right]$ for $r > a$. The displacement continuity at $r = a$ then requires that $C_1 = -\frac{E_{2D}au_s}{(1+\nu)}\left[1 - \left(\frac{a}{L_m}\right)^2\right]^{-1}$. Following the same process in Eq. (14-16), we obtain $u_s = u_0 - h^2/a$ and $u_0 = \frac{(3-\nu)h^2}{4a}$, which then leads to Eq. (1) for the height-to-radius ratio with $\phi = \frac{6L_m^2(1-\nu)}{5L_m^2(1-\nu)+3a^2(1+\nu)}$. Note that, in this case, ϕ depends on the ratio L_m/a. For a constant

liquid volume ($V = \pi a^2 h/2$), the coefficient ϕ can be determined by solving a nonlinear algebraic equation as:

$$\phi + \frac{3(1+\nu)}{5(1-\nu)}\left(\frac{2V}{\pi L_m^3}\right)^{\frac{2}{3}}\left(\frac{E_{2D}}{\Delta\gamma}\right)^{\frac{1}{6}}\phi^{\frac{5}{6}} = \frac{6}{5} \tag{17}$$

Apparently in this case, the height-to-radius ratio of the blister depends on the size of the membrane through the ratio L_m^3/V. As shown in Fig. S3, as $L_m^3/V \to \infty$, the coefficient ϕ approaches the weak shear limit ($\phi = \frac{6}{5}$). However, since the size of membrane is limited in MD simulations, Eq. (17) predicts a smaller value for ϕ, and hence a smaller height-to-radius ratio for the blister by Eq. (1). Fig. S3 plots the radius of the blister as a function of the membrane size, both normalized by $V^{1/3}$. Clearly, the blister radius decreases with increasing adhesion energy ($\Delta\gamma = \Gamma - \gamma_w(\cos\theta_s + \cos\theta_m)$). Meanwhile, the radius increases slightly with decreasing L_m. In any case, the radius should be no greater than the half side length of the membrane, i.e., $a \le L_m$. In the extreme case when $a = L_m$, the edge of the blister is fixed with no sliding, and the solution reduces to the strong shear limit with $\phi \approx 0.6$ for the case of a graphene monolayer as the membrane.

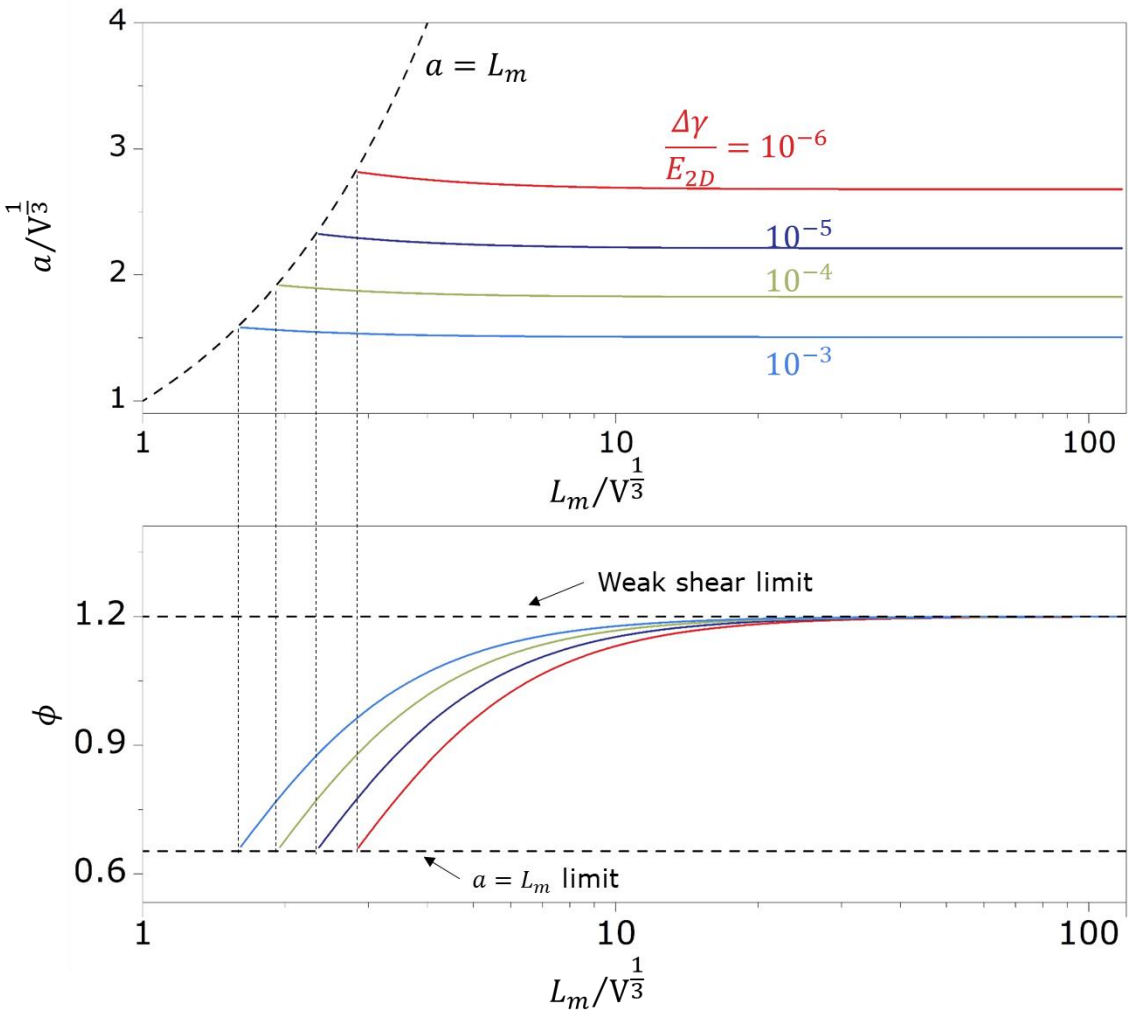

Figure S3. Effect of the finite membrane size in MD simulations on the blister radius a and the coefficient ϕ in the height-to-radius ratio equation (Eq. (1)).

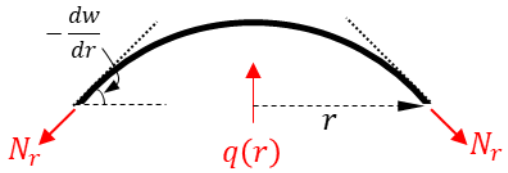

Figure S4. Side view of the equilibrium of stress resultants for a membrane blister.

In addition, as illustrated in Fig. S4, the force equilibrium leads to:

$$q \simeq -\frac{2}{a}\left(N_r \frac{dw}{dr}\right)_{r=a}, \tag{18}$$

where the radial stress can be calculated by Eq. (14) using the strain components in Eqs. (4) and (5). With Eqs. (2) and (3), we obtain the average pressure inside the blister in the following form:

$$q = \eta \frac{E_{2D} h^3}{a^4}, \tag{19}$$

where η is $\frac{2}{1-\nu}$ and 1 for strong and weak shear limit and η is $\frac{L_m^2(1-\nu)+a^2(1+\nu)}{L_m^2(1-\nu)}$ for modified weak shear limit in MD simulations. Therefore, the liquid pressure inside the blister may be estimated by Eq. (19) in terms of the blister radius and height. This could be of interest for applications using blisters of 2D materials for the study of interface-confined high-pressure chemistry (11-13).

Hencky's analysis with finite shear. Next we present a more rigorous analysis for the liquid-filled blisters following Hencky's approach (6, 7). The shear interactions between the membrane and the substrate is represented by a finite interfacial shear stress in the supported region ($a < r < \rho a$), where both the blister radius (a) and the outer radius of the shear zone (ρa) are to be determined depending on the liquid volume and the shear stress. The membrane size is assumed to be large so that the shear zone does not reach the edge of the membrane (Fig. S5). The membrane outside the sliding zone ($r > \rho a$) is not deformed or stressed. Since h/a is typically small, the membrane is assumed to conform to the liquid ($r < a$) with a uniform pressure, similar to the gas-filled blisters. Outside the blister, the substrate-supported membrane is subject to in-plane stresses and a constant interfacial shear stress in the shear zone ($a < r < \rho a$). The two parts are coupled at the edge of the blister ($r = a$) by the continuity conditions in terms of the stress and displacement.

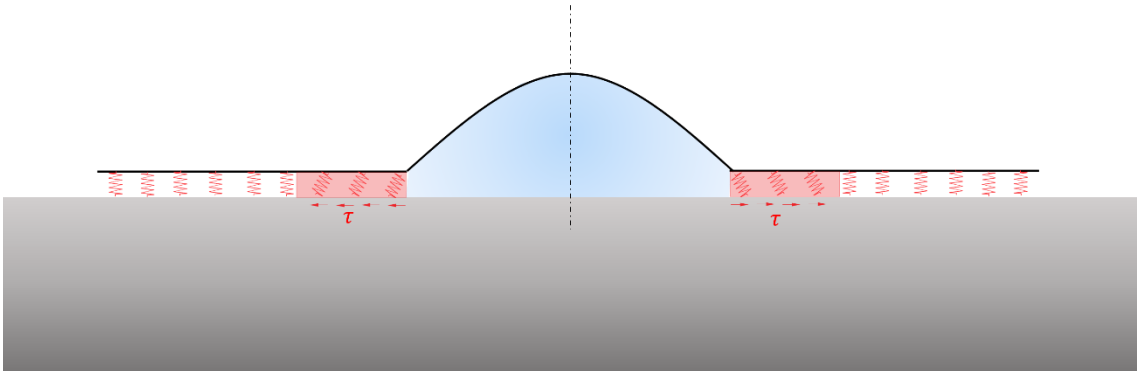

Figure S5. Schematic illustration of water-filled 2D materials blister on a rigid substrate.

The mechanical equilibrium of the bulged membrane ($r < a$) over the liquid requires that:

$$\frac{d}{dr}(rN_r) - N_\theta = 0, \tag{20a}$$

$$\frac{d}{dr}\left(rN_r \frac{dw}{dr}\right) + qr = 0, \tag{20b}$$

where q is the intensity of the transverse loading (*i.e.* the pressure difference across the membrane). These equations assume axisymmetric deformation and ignore bending rigidity of the membrane. With linear elasticity and nonlinear kinematics, Eqs. (20a) and (20b) can be combined into one nonlinear equation:

$$N_r^2 \frac{d}{dr}\left[\frac{1}{r}\frac{d}{dr}(r^2 N_r)\right] + \frac{E_{2D}q^2}{8} r = 0. \tag{21}$$

Following Hencky's approach (6, 7), the solution to Eqs. (20-21) is assumed to take the polynomial form as:

$$N_r(r) = \left(\frac{E_{2D}q^2a^2}{64}\right)^{\frac{1}{3}} \sum_{n=0}^{\infty} b_{2n} \left(\frac{r}{a}\right)^{2n}, \tag{22a}$$

$$N_\theta(r) = \left(\frac{E_{2D}q^2a^2}{64}\right)^{\frac{1}{3}} \sum_{n=0}^{\infty} (2n+1) b_{2n} \left(\frac{r}{a}\right)^{2n}, \tag{22b}$$

$$w(r) = \left(\frac{qa^4}{E_{2D}}\right)^{\frac{1}{3}} \sum_{n=0}^{\infty} a_{2n} \left[1 - \left(\frac{r}{a}\right)^{2n+2}\right], \tag{23}$$

where seven terms (n = 0-6) are typically included in each polynomial. Substituting Eq. (22a) into Eq. (21), all the coefficients b_{2n} can be determined in terms of one parameter, b_0. That is, $b_2 = -\frac{1}{{b_0}^2}; b_4 = -\frac{2}{3{b_0}^5}; b_6 = -\frac{13}{18{b_0}^8};\ b_8 = -\frac{17}{18{b_0}^{11}};\ b_{10} = -\frac{37}{27{b_0}^{14}};\ b_{12} = -\frac{1205}{567{b_0}^{17}}$. Similarly, substituting Eq. (23) into Eq. (20b) yields: $a_0 = \frac{1}{b_0}; a_2 = \frac{1}{2{b_0}^4};\ a_4 = \frac{5}{9{b_0}^7};\ a_6 = \frac{55}{72{b_0}^{10}};\ a_8 = \frac{7}{6{b_0}^{13}};\ a_{10} = \frac{205}{108{b_0}^{16}};\ a_{12} = \frac{17051}{5292{b_0}^{19}}$. Given a and q, the coefficient b_0 can be determined numerically, depending on Poisson's ratio of the membrane and boundary conditions. For instance, $b_0 = 1.67$ was obtained for an elastic membrane clamped at the edge with $\nu = 0.165$ (for graphene).

Outside the blister, the supported 2D membrane is constrained to in-plane deformation with axisymmetry and a constant interfacial shear stress (frictional force per unit area), τ, which opposes sliding. For a given blister pressure or volume, there would exist an annular interfacial sliding zone ($a < r < \rho a$), beyond which there would be no sliding and thus zero shear stress. Assuming no buckling or any out-of-plane deflection (*i.e.* $w = 0$) for the supported membrane outside the blister, the in-plane equilibrium equation is (5):

$$\frac{d}{dr}(rN_r) - N_\theta + \tau r = 0. \tag{24}$$

With linear elasticity and in-plane kinematics, Eq. (24) can be re-written as:

$$\frac{d}{dr}\left[N_r + \frac{d}{dr}(rN_r)\right] = -(2+\nu)\tau. \tag{25}$$

Solving Eqs. (24) and (25) with the boundary condition at $r = \rho a$, where the in-plane stresses are zero ($N_r = N_\theta = 0$), we obtain:

$$N_r = \tau a\left[(2+\nu)\left(-\frac{1}{3}\frac{r}{a} - \frac{\nu-1}{6(2+\nu)}\rho^3\frac{a^2}{r^2}\right) + \frac{1+\nu}{2}\rho\right], \tag{26a}$$

$$N_\theta = \tau a\left[(2+\nu)\left(-\frac{1+2\nu}{3(2+\nu)}\frac{r}{a} + \frac{\nu-1}{6(2+\nu)}\rho^3\frac{a^2}{r^2}\right) + \frac{1+\nu}{2}\rho\right]. \tag{26b}$$

At the edge of the blister ($r = a$), the radial stress and displacement are continuous. As a result, both the strain and stress components are continuous, *i.e.*, $N_r^{in} = N_r^{out}$ *and* $N_\theta^{in} = N_\theta^{out}$ *at* $r = a$. Based on Eq. (22) for the bulged membrane and Eq. (26) for the membrane outside the blister, the continuity conditions at the edge of the blister lead to:

$$\tau a\left[(2+\nu)\left(-\frac{1}{3} - \frac{\nu-1}{6(2+\nu)}\rho^3\right) + \frac{1+\nu}{2}\rho\right] = \left(\frac{E_{2D}q^2a^2}{64}\right)^{\frac{1}{3}}\left(b_0 - \frac{1}{{b_0}^2} - \frac{2}{3{b_0}^5} - \cdots\right), \tag{27a}$$

$$\tau a\left[(2+\nu)\left(-\frac{1+2\nu}{3(2+\nu)} + \frac{\nu-1}{6(2+\nu)}\rho^3\right) + \frac{1+\nu}{2}\rho\right] = \left(\frac{E_{2D}q^2a^2}{64}\right)^{\frac{1}{3}}\left(b_0 - \frac{3}{{b_0}^2} - \frac{10}{3{b_0}^5} - \cdots\right). \tag{27b}$$

Given τ, a and q, Eq. (27) can be solved to obtain the Hencky constant b_0 and the ratio ρ for the outer radius of the interfacial sliding zone.

For a liquid-filled blister with a constant volume (V), we define a length scale as $L_w = V^{1/3}$. By integrating the deflection in Eq. (23), the volume is related to the pressure difference as:

$$V = 2\pi \int_0^a w(r)\, r dr = \frac{2\pi a^{10/3} q^{1/3}}{E_{2D}^{1/3}} \sum_n a_{2n} \left(\frac{n+1}{2n+4}\right). \tag{28}$$

Thus, the normalized pressure difference is:

$$\bar{q} = \frac{qL_w}{E_{2D}} = \left(\frac{L_w}{a}\right)^{10} \left[2\pi \sum_n a_{2n} \left(\frac{n+1}{2n+4}\right)\right]^{-3}. \tag{29}$$

For given τ, a and V, Eq. (27) can be solved to obtain b_0 and ρ, both depending on three dimensionless parameters: ν, $\bar{\tau} = \frac{\tau L_w}{E_{2D}}$, and $\bar{a} = \frac{a}{L_w}$. Moreover, for a particular membrane material with a constant Poisson's ratio ν, b_0 and ρ depend on a single parameter: $\xi = \bar{\tau}\,\bar{a}^7$. In Fig. S6, we plot b_0 and ρ versus ξ for graphene ($\nu = 0.165$). Clearly, when $\xi \to \infty$ (*i.e.* $\tau \to \infty$ or $\bar{a} \to \infty$), the results approach the strong shear limit without any sliding (*i.e.* $\rho = 1$ and $b_0 = 1.67$). With a finite interfacial shear stress τ, ρ increases as ξ decreases. In the weak shear limit ($\xi \to 0$), $\rho \to \infty$ and $b_0 \to 1.47$.

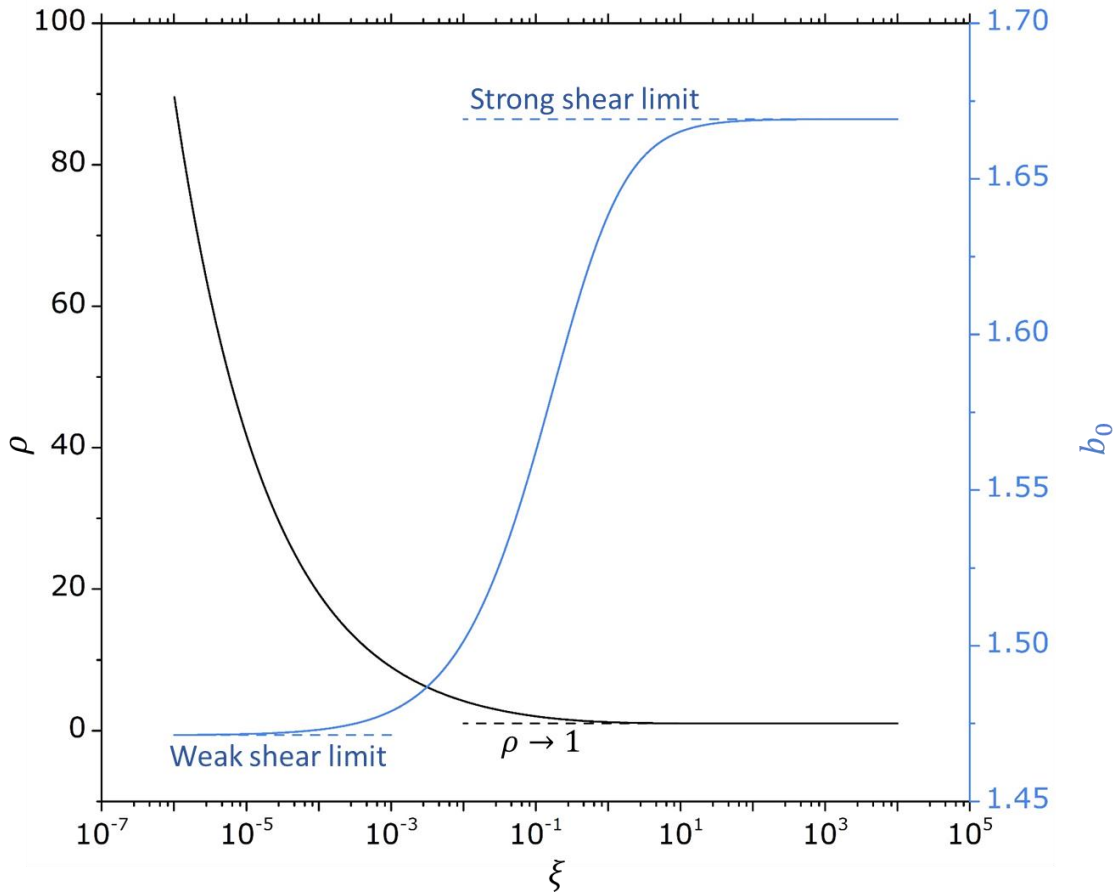

Figure S6. The radius ratio ρ of the interfacial sliding zone (black lines) and Hencky constant b_0 (blue lines) as a function of ξ.

According to Eq. (23), the blister height, $h = w|_{r=0}$, and the height-to-radius ratio is:

$$\frac{h}{a} = C_1 \left(\frac{qa}{E_{2D}}\right)^{\frac{1}{3}} = C_1\, \bar{a}^{-3} \left[2\pi \sum_n a_{2n} \left(\frac{n+1}{2n+4}\right)\right]^{-1}. \tag{30}$$

where $C_1 = \sum_n a_{2n} = \frac{1}{b_0} + \frac{1}{2{b_0}^4} + \frac{5}{9{b_0}^7} + \cdots$. By Eq. (30), h/a depends on both $\bar{a}$ and $\bar{\tau}$. Similarly, by Eq. (29), the normalized pressure difference $\bar{q}$ depends on $\bar{a}$ and $\bar{\tau}$ as well. For a given $\bar{\tau}$, $\bar{q}$ is related to $\bar{a}$ and then to h/a. It is thus possible to determine the pressure inside the blister based on the measurement of the height and radius of the blisters. Fig. S7 plots $\frac{qa}{E_{2D}}$ $(= \bar{q}\bar{a})$ as a function of h/a for blisters with various interfacial shear stresses. Note that, Eq. (30) can be rewritten as:

$$q = \eta(\xi, \nu) \frac{E_{2D} h^3}{a^4} \tag{31}$$

where $\eta(\xi, \nu) = C_1^{-3}$. We find that the $\frac{qa}{E_{2D}} - \frac{h^3}{a^3}$ curves collapse when $\bar{\tau} \geq 1$ (strong shear) and $\bar{\tau} \leq 10^{-4}$ (weak shear). Eq. (31) is similar to Eq. (19) by the simple analysis, but it is more accurate. In particular, for the strong and weak shear limits, the simple analysis underestimates the pressure significantly.

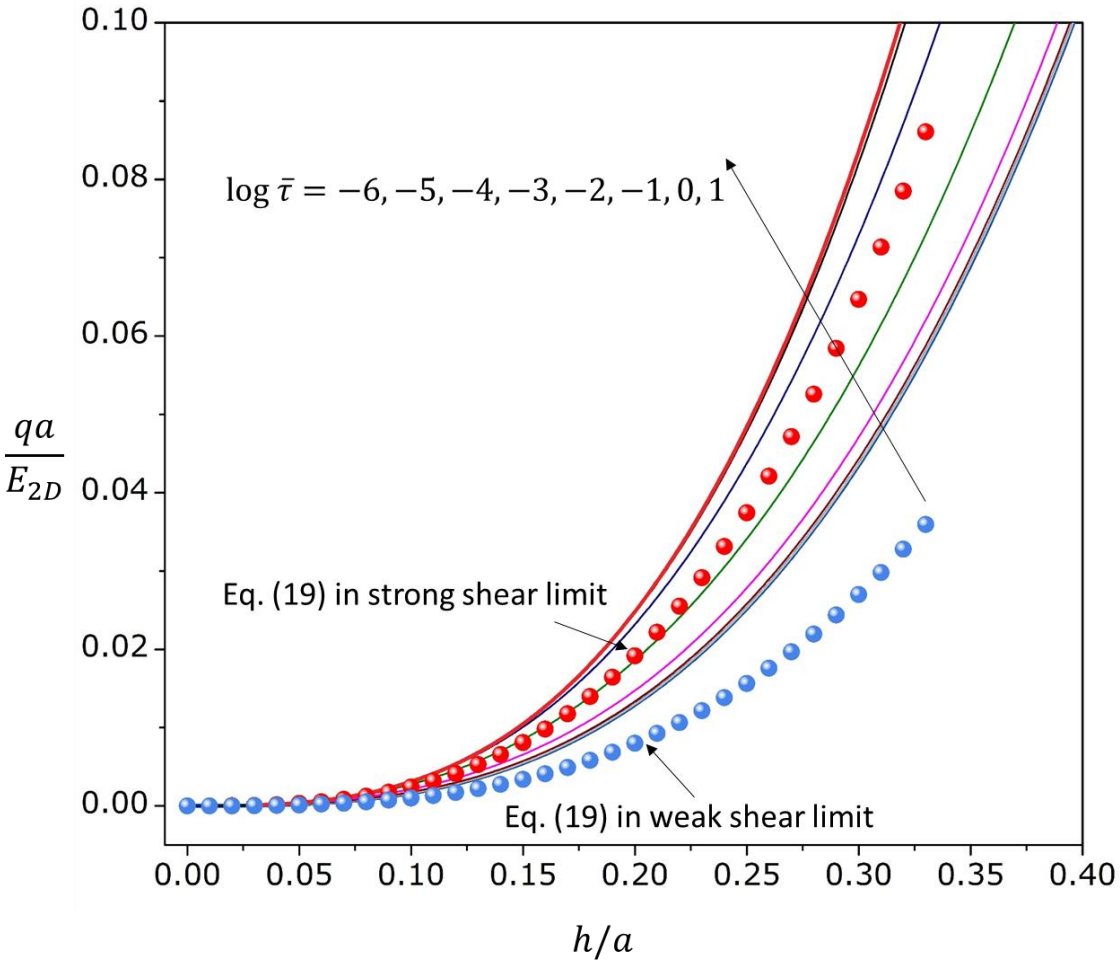

Figure S7. The dimensionless pressures as a function of height/radius ratio under various shear stress. Blue and red dots are from the simple analysis.

For given τ and V, the blister radius is determined by minimizing the total free energy of the blister, including the elastic strain energy of the membrane and the interfacial energy. With the membrane stresses in Eq. (22), the strain energy for the bulged membrane can be obtained as

$$F_{e1}(a) = 2\pi \int_0^a U_S(r)\, r dr = E_{2D} L_w^2 \left(\frac{L_w}{a}\right)^{10} f_1(\xi, \nu). \tag{32}$$

Similarly, the strain energy for the supported membrane can be obtained with the in-plane stresses in Eq. (26) as

$$F_{e2}(a) = 2\pi \int_a^{\rho a} U_S(r)\, r dr = E_{2D} L_w^2 \left(\frac{L_w}{a}\right)^{10} f_2(\xi, \nu). \tag{33}$$

Relative to a reference state of the membrane on the substrate without liquid, the interfacial energy of the liquid-filled blister is:

$$F_i(a) = \pi a^2(\gamma_{ws} - \gamma_{ms}) + \gamma_{wm}A', \tag{34}$$

where A' is the area of blister surface, i.e.,

$$A' = 2\pi \int_0^a \sqrt{1 + \left(\frac{dw}{dr}\right)^2}\, rdr = C_3\pi a^2, \tag{35}$$

and C_3 is a constant that depends on b_0. With $\Delta\gamma = \gamma_{mw} + \gamma_{sw} - \gamma_{ms}$, we have

$$F_i(a) = \pi a^2 \Delta\gamma \left[1 + (C_3 - 1)\frac{\gamma_{wm}}{\Delta\gamma}\right]. \tag{36}$$

To minimize the total free energy, we set

$$\bar{F}(\bar{a}, \bar{\tau}, \nu) = \frac{F_{e1}+F_{e2}+F_i}{E_{2D}L_w^2} = [f_1(\xi, \nu) + f_2(\xi, \nu)]\bar{a}^{-10} + \frac{\pi\Delta\gamma}{E_{2D}}\left[1 + (C_3 - 1)\frac{\gamma_{wm}}{\Delta\gamma}\right]\bar{a}^2, \tag{37}$$

and

$$\frac{\partial \bar{F}}{\partial \bar{a}} = 0, \tag{38}$$

by which $\bar{a} = a/L_w$ can be solved as a function of $\bar{\tau}, \nu$, $\frac{\Delta\gamma}{E_{2D}}$ and $\frac{\gamma_{wm}}{E_{2D}}$. Then, by Eq. (30), the ratio h/a can be obtained as well. Since $C_3 \sim 1 + \boldsymbol{O}(h^2/a^2)$, here we neglect the effects of $\frac{\gamma_{wm}}{\Delta\gamma}$ due to the small aspect ratio observed in our experiments, and only examine the effect of shear stress on h/a in Fig. S8. Similar to the observation in Fig. S7, $h/a - \Delta\gamma/E_{2D}$ curves collapse when $\bar{\tau} \geq 1$ (strong shear) and $\bar{\tau} \leq 10^{-4}$ (weak shear) and show agreement with the simple analysis under small h/a (< 0.15). However, slight deviations can be observed under high aspect ratio, implying the limitation of our simple analysis for large deformation.

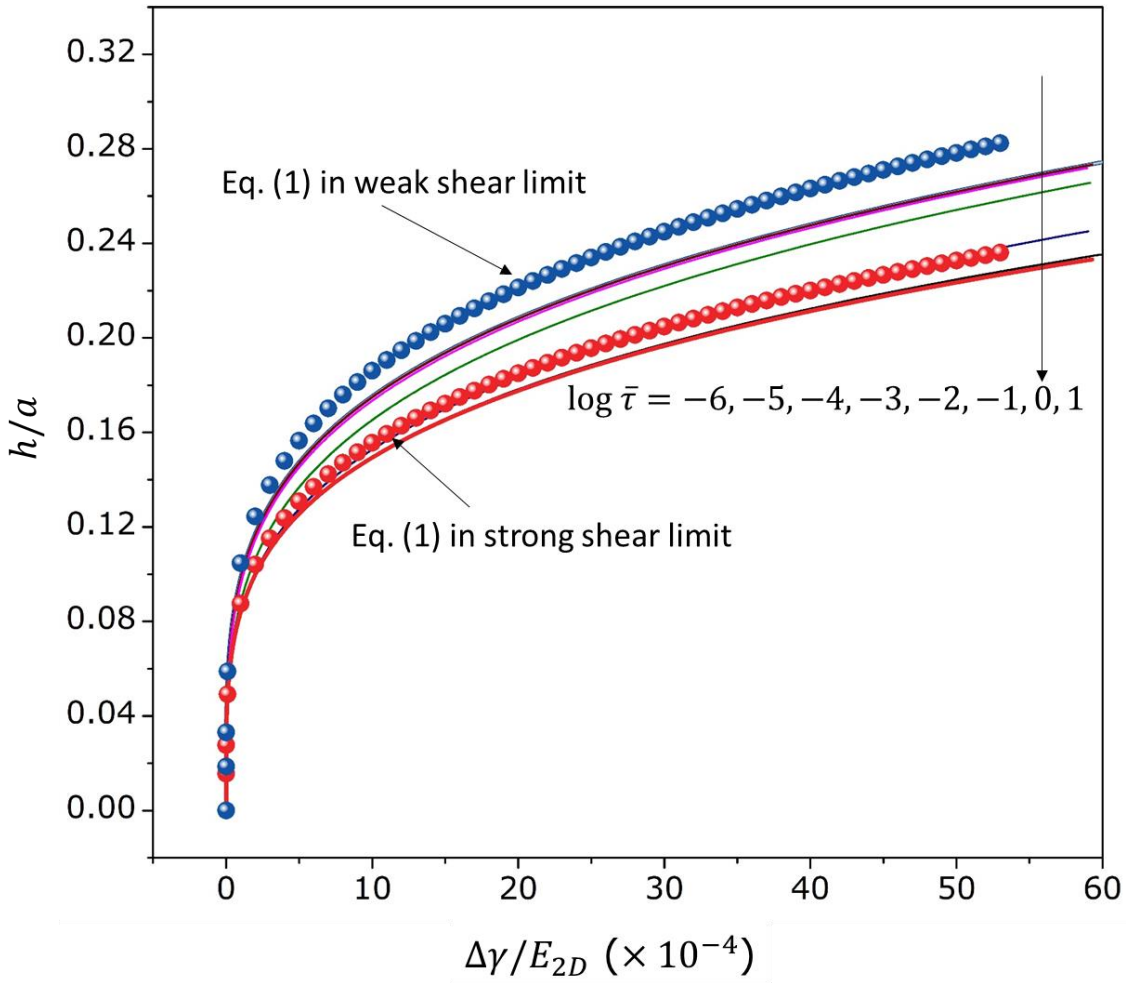

Figure S8. The dependency of the aspect ratio on $\Delta\gamma/E_{2D}$ for different shear stresses. Blue and red dots are from the simple analysis.

Next, we consider the effect of finite membrane size ($\rho = \rho_0$). As the 2D membranes in experiments typically have finite lateral sizes (here, defined as $\rho_0 a$), the sliding zone around a blister could grow to the boundary of the membrane if the interface is relatively weak or if the blister is located near the edge of a membrane. In these cases, the sliding zone radius ratio ρ would become fixed once it reaches the critical value ρ_0 as shown in Fig. S9. Unlike the previous case with $N_r = N_\theta = 0$ at $r = \rho a$, the boundary condition at $r = \rho_0 a$ is slightly different, *i.e.*, $N_r = 0$ but $N_\theta \neq 0$. Thus, for a finite outer boundary, the Eq. (25) can be solved exactly to obtain:

$$N_r = \tau a \left[-\frac{(2+\nu)}{3}\frac{r}{a} + A_0 \left(\frac{a^2}{r^2} - \frac{1}{{\rho_0}^2} \right) + \frac{(2+\nu)}{3}\rho_0 \right] \tag{39a}$$

$$N_\theta = \tau a \left[-\frac{(1+2\nu)}{3}\frac{r}{a} + A_0 \left(-\frac{a^2}{r^2} - \frac{1}{{\rho_0}^2} \right) + \frac{(2+\nu)}{3}\rho_0 \right] \tag{39b}$$

where A_0 is a dimensionless constant to be determined. Then, based on Eqs. (22) for the bulged membrane over the blister and Eqs. (39) for the supported membrane, the continuity conditions at the edge of blister ($r = a$) lead to:

$$\tau a\left[-\frac{(2+\nu)}{3}+A_0\left(1-\frac{1}{{\rho_0}^2}\right)+\frac{(2+\nu)}{3}\rho_0\right]=\left(\frac{Etq^2a^2}{64}\right)^{\frac{1}{3}}\left(b_0-\frac{1}{{b_0}^2}-\frac{2}{3{b_0}^5}-\cdots\right) \quad (40a)$$

$$\tau a\left[-\frac{(1+2\nu)}{3}+A_0\left(-1-\frac{1}{{\rho_0}^2}\right)+\frac{(2+\nu)}{3}\rho_0\right]=\left(\frac{Etq^2a^2}{64}\right)^{\frac{1}{3}}\left(b_0-\frac{3}{{b_0}^2}-\frac{10}{3{b_0}^5}-\cdots\right) \quad (40b)$$

Combining Eq. (29) and Eq. (40) we can solve for the constant A_0 and Hencky constant b_0, with given ν, $\bar{\tau}$, and $\bar{a}$. Following the same process, we can calculate the total free energy $\bar{F}(\bar{a},\bar{\tau},\nu)$ and determine $\bar{a}$ by minimizing the free energy. The ratio h/a can still be determined by Eq. (30), but with b_0 depending on ρ_0. In Fig. S9, we demonstrated the effect of ρ_0 on the ratio h/a. We find that the finite size effect is negligible when $\rho_0 > 4$, which can be readily satisfied experimentally by choosing 2D materials blisters not located close to the edge of a membrane.

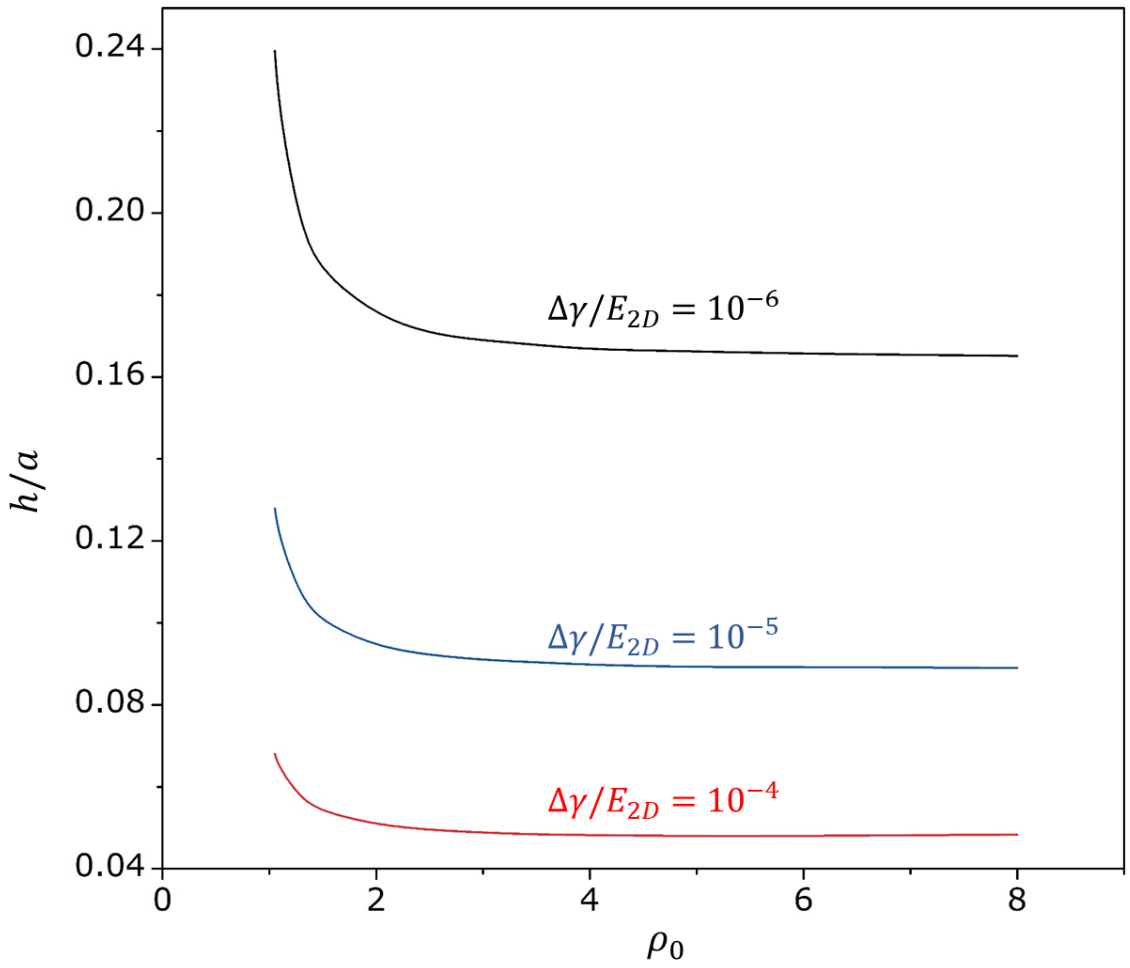

Figure S9. The aspect ratio as function of ρ_0. The shear stress used for this demonstration is $\bar{\tau} = 10^{-5}$, with which interface is more sensitive to the lateral size compared with strong shear.

Section 3: MD simulations.

We performed classical MD simulations for water blisters trapped between SiO_2 and graphene using LAMMPS (14). A square-shaped graphene membrane (L ~ 30 nm) was placed on top of a flat substrate surface, with water molecules in between. MD simulations were carried out in NVT ensemble with periodic boundary conditions at 300K, where the temperature was controlled by a Nose-Hoover thermostat. The integration time step was 1 fs. The in-plane dimension of the periodic box was set by the size of the graphene sheet (~30 nm), and the thickness of the periodic box was 20 nm so as to keep periodic images in the thickness direction from interacting with each other. The substrate was modeled as a rigid surface placed at z = -0.316 nm so that the average position of the carbon atoms in the graphene would be around z = 0 if no water molecules are trapped in between. Initially, a number of water molecules were placed as a block between the substrate and the graphene sheet. Then, the system was relaxed for 2 ns to form a blister. Fig. S10 shows a snapshot of a graphene blister with 2700 water molecules, shaped like a spherical cap by the top and side views. We retrieved the blister configuration by sampling 10 snapshots evenly after 1 ns relaxation. The blister height was measured as the difference between the largest z positon of the carbon atoms and the average z position (~0) outside the blister edge (see Fig. S10B). The blister diameter was measured as the maximum span distance for the carbon atoms with z > 0.1 nm. The height-radius ratio (h/a) was calculated by averaging over the 10 snapshots with an error bar for the standard deviation.

The second-generation reactive empirical bond-order (REBO) potential (15) was used for the carbon-carbon interactions in graphene. The TIP4P/2005 model (16) was used for interactions between water molecules, which has been shown to accurately predict the surface tension of water (17). A fictitious surface interacting with both graphene and water molecules was used to represent the rigid substrate (18). The interaction potential between carbon atoms of graphene and the surface was specified in form of Eq. (41) with two parameters (ε_{CS} and δ_{CS}),

$$U_{CS} = \varepsilon_{CS}\left[\frac{2}{15}\left(\frac{\delta_{CS}}{r_{CS}}\right)^9 - \left(\frac{\delta_{CS}}{r_{CS}}\right)^3\right] \quad (41),$$

where r_{CS} is the distance between each carbon atom and the surface. The equilibrium separation and adhesion energy of the graphene/substrate interface can then be obtained as

$$h_{GS} = \left(\frac{2}{5}\right)^{1/6} \delta_{CS} \tag{42},$$

$$\Gamma_{GS} = \frac{4\sqrt{10}}{9\sqrt{3}} \frac{\varepsilon_{CS}}{r_0^2} \tag{43},$$

where $r_0 = 0.142$ nm is the bond length of graphene. Here, we used $\delta_{CS} = 0.368$ nm so that h_{GS} = 0.316 nm, as predicted by DFT calculations for graphene on SiO_2 (19). The adhesion energy Γ_{GS} was varied between 0.1 and 0.5 J/m^2, as the typical range from both experiments and theoretical calculations (19-25).

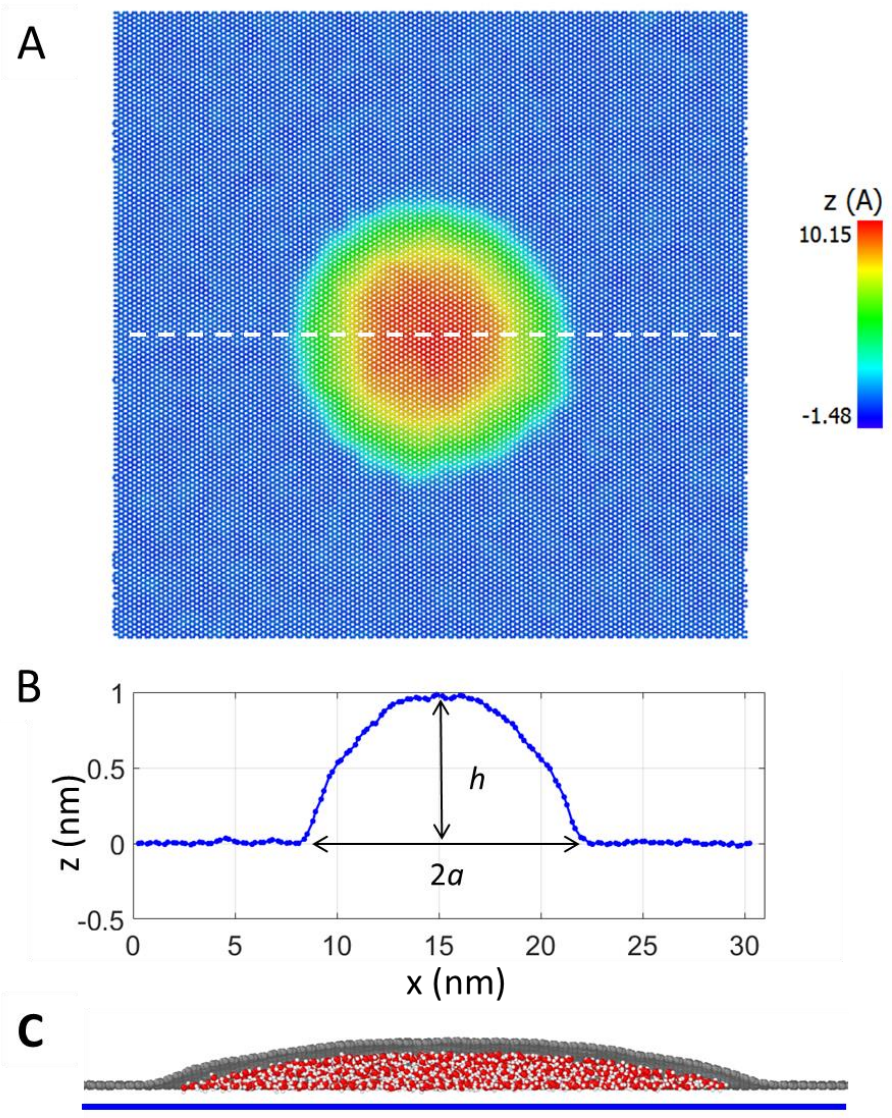

Figure S10. MD simulation of a graphene blister with 2700 water molecules. The adhesion energy was Γ_{GS} = 0.242 J/m^2, while the water contact angles were 60^{o}and 40^{o}for graphene and the substrate, respectively.

(*A*) A top view snapshot of the blister, with color contour for the *z*-position of the carbon atoms in graphene; (*B*) A height profile along a line scan (dashed line in A) across the blister; (*C*) A cross-sectional view of the blister, showing the water molecules (oxygen in red and hydrogen in white) between graphene (carbon in gray) and the substrate surface (blue line).

The interactions between water molecules and the substrate surface were modeled similarly by a potential function with two parameters (ε_{OS} and δ_{OS}) for the interactions between the oxygen atoms of water and the surface as

$$U_{WS} = \varepsilon_{OS}\left[\frac{2}{15}\left(\frac{\delta_{OS}}{r_{OS}}\right)^9 - \left(\frac{\delta_{OS}}{r_{OS}}\right)^3\right] \quad (44),$$

while the interactions between the hydrogen atoms of water and the surface were ignored. We also let $\delta_{OS} = 0.368$ nm so that the equilibrium separation between the water molecules and the surface is identical to the graphene/substrate interface. The parameter ε_{OS} can be varied to yield different water contact angles for the substrate. We performed MD simulations of a water droplet on the surface to determine the contact angle as a function of ε_{OS} (Fig. S11). For this purpose, the water surface was re-constructed at 10 snapshots of the simulation by the alpha-shape method (26) with a virtual probe sphere of radius 0.4 nm using OVITO (27). The surface area and the water volume were calculated, with which the averaged contact angle (θ_s) was calculated by assuming a spherical cap shape for the droplet. The effect of the number of water molecules on the contact angle was examined and found to be insignificant in the range from $N = 100$ to $N = 4500$. Based on this result, we chose $\varepsilon_{OS} = 0.08$ eV to have a water contact angle of ~40^0 for the substrate.

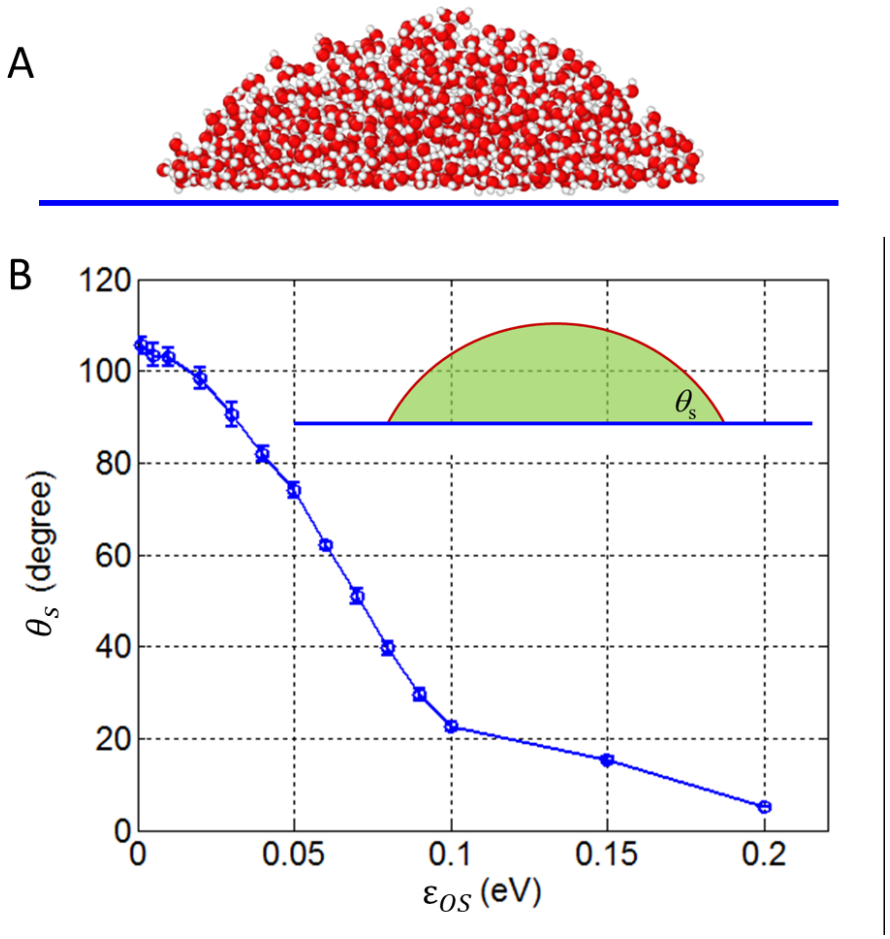

Figure S11. (*A*) A snapshot of a water droplet on a substrate surface with N = 900 and ε_{OS} = 0.08 eV, where the contact angle is around 40°. (*B*) Water contact angle of substrate as a function of ε_{OS} .

Next, for the interactions between water and graphene, previous first-principle calculations (28, 29) have shown that the interactions between graphene and water are dominated by dispersion interactions. Werder et al. (30) calibrated a set of parameters for the interactions between the oxygen atoms of water and the carbon atoms of graphene using the LJ potential in its standard form:

$$U_{GW} = 4\varepsilon_{CO}\left[\left(\frac{\delta_{CO}}{r_{CO}}\right)^{12} - \left(\frac{\delta_{CO}}{r_{CO}}\right)^{6}\right] \quad (45).$$

With fitted parameters $\delta_{CO} = 0.319$ nm and $\varepsilon_{CO} = 4.07$ meV, they obtained a water contact angle of around 90° for graphene (30, 31). However, recent studies found that the water contact angle is

around 60° for pristine graphene without air-borne contamination (32). In this study, we used ε_{CO} = 6.0 meV so that the predicted water contact angle is 60° for graphene. Fig. S12A shows a snapshot of a water droplet on graphene by MD simulations, and Fig. S12B shows the water contact angle as a function of ε_{CO} based on the MD simulations. It is noted that, by adjusting the interaction parameters between water and graphene, the wetting behavior of graphene can be described without affecting the mechanical properties of graphene itself. For the other 2D materials, although we did not perform MD simulations in the present study, the continuum model as verified for graphene blisters was applied with their corresponding wetting and mechanical properties.

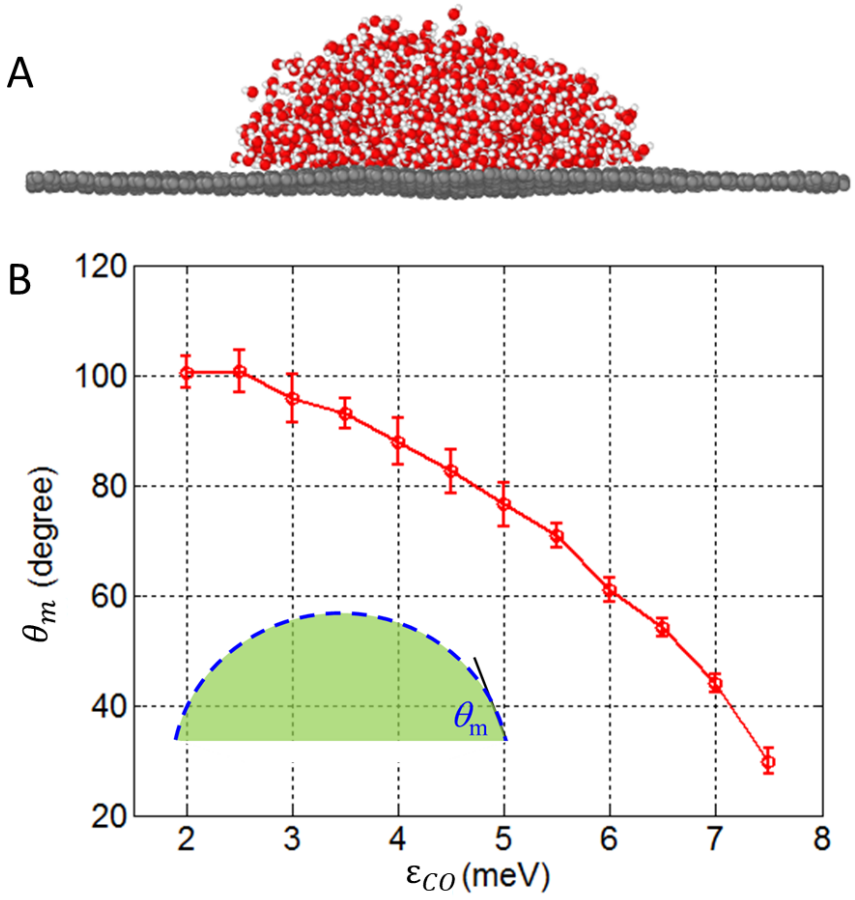

Figure S12. (*A*) A snapshot of a water droplet on graphene with N = 1000 and ε_{CO} = 6.0 meV, where the contact angle is around 60°. (*B*) Water contact angle of graphene as a function of ε_{CO} by MD simulations.

Breakdown of the continuum model. By assuming the trapped water in the blister as a continuum liquid, the model predicts the shape of the blister close to a spherical cap. However, our MD simulations showed that the blister may take a different shape when the membrane/substrate adhesion energy was relatively low and the number of water molecules was small. Instead of a spherical cap, the top of the blister was flat, indicating that the water molecules formed discrete layers. In this case, the continuum model breaks down because the trapped water cannot be treated as a continuum liquid. It is found that the breakdown occurs when the height of the blister predicted by the continuum model drops below the thickness of three water monolayers. A simple analysis is presented below to predict the breakdown condition in terms of the adhesion energy and the number of water molecules.

By the simple continuum model, the water volume in the blister is approximately

$$V = \frac{1}{2}\pi h a^2 \tag{46}.$$

The number of water molecules can then be found as

$$N = \rho V \tag{47},$$

where ρ is the number density of water, which equals 33.2 nm^{-3} at T = 300K by the TIP4P/2005 model in MD simulations(33). Thus, the height of the blister can be written as

$$h = \left(\frac{2N}{\pi\rho}\right)^{1/3}\left(\frac{h}{a}\right)^{2/3} = \left(\frac{2N}{\pi\rho}\right)^{1/3}\left(\phi\frac{\Gamma-\gamma_w(\cos\theta_m+\cos\theta_s)}{E_{2D}}\right)^{\frac{1}{6}} \tag{48},$$

where Eq. (1) is used for the ratio $\frac{h}{a}$. Note that, under the condition of MD simulations, the parameter ϕ is given by Eq. (17) as a function of Γ and V (or N). For a given adhesion energy Γ and the water contact angles, the blister height decreases with decreasing number of water molecules as shown in Fig S13A. When the height drops below a critical level, the continuum model breaks down and the water molecules form discrete layers instead. The critical height is roughly three times the thickness of a water monolayer, which is estimated as $h_c = 3\rho^{-1/3} = 0.93\ nm$. Thus, the continuum model holds only when $h > h_c$. For Γ = 0.242 J/m^2, the continuum model breaks down when the number of water molecules N < 1690, while for Γ = 0.1 J/m^2 the breakdown occurs for N < 7640. By setting $h = h_c$, we obtain the critical condition in terms of Γ and N shown as the blue curve in Fig. S13B. Furthermore, when the number of water molecules

drops below a second critical level ($\sim 2\rho^{-1/3} = 0.62\ nm$), we may expect the water molecules to form a single monolayer. However, since the continuum model has already broken down, it is not possible to predict exactly when the water monolayer would form.

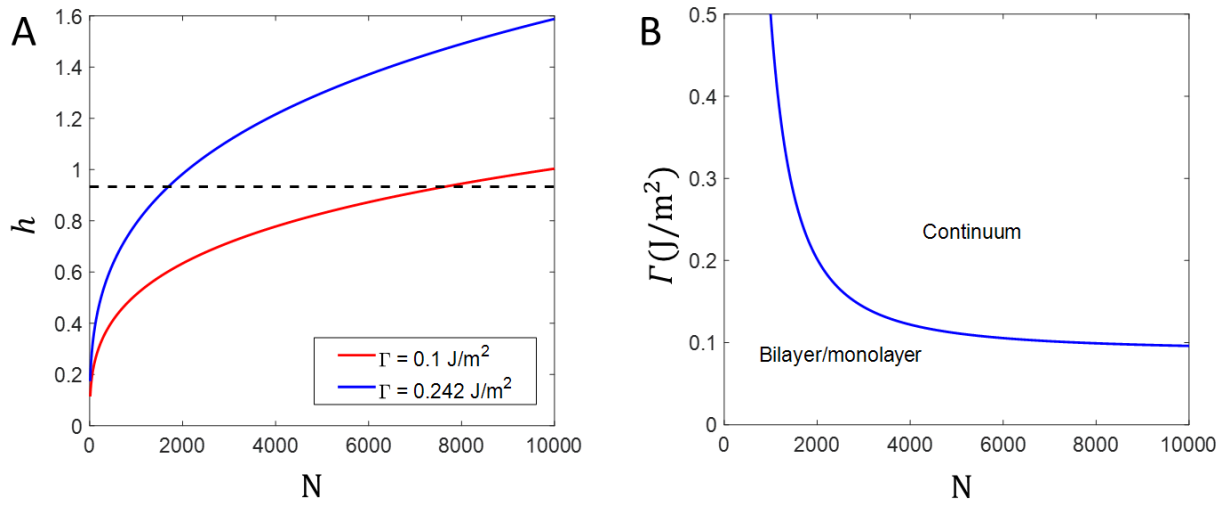

Figure S13. (*A*) The height of graphene blister as a function of the number of water molecules, predicted by the continuum model for Γ_{GS} = 0.1 J/m^2 and 0.242 J/m^2, where the dashed line indicate the critical height for the continuum model. (*B*) The breakdown limit for the continuum model, in terms of the adhesion energy Γ_{GS} and the number of water molecules *N* with the water contact angles being 60° and 40° for graphene and the substrate, respectively.

The formation of layered water molecules was observed in MD simulations. We conducted MD simulations with different number of water molecules ranging from N = 50 to N = 4500 for different values of the adhesion energy Γ. The *h/a* ratio varying with respect to the number of water molecules is plotted in Fig. S14, along with analytical predictions by the modified weak shear continuum model. For Γ = 0.242 J/m^2, the MD results are in close agreement with the continuum prediction for N > 1600, below which the continuum model breaks down. The water molecules form a bilayer structure for 400 < N < 1600 and form a monolayer for N < 400. At each transition, from continuum to bilayer or from bilayer to monolayer, the ratio *h/a* drops abruptly and then increases with decreasing *N*. This can be understood as the blister height changes discontinuously at the transition, whereas the blister radius decreases almost continuously with decreasing N. For Γ = 0.1 J/m^2, however, the continuum regime was not reached for the limited number of water molecules in the MD simulations (N < 5000). In this case, the water molecules form a bilayer structure for N > 400 and transition to a monolayer for N < 400.

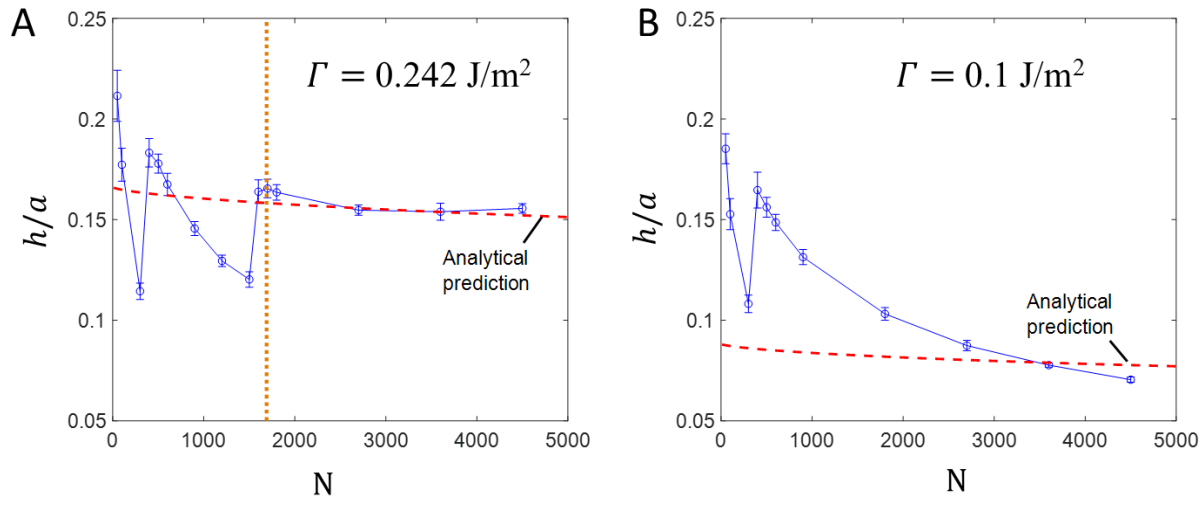

Figure S14. Blister aspect ratio for different numbers of water molecules, for Γ_{GS} = 0.242 J/m^2 (*A*) and 0.1 J/m^2 (*B*) with water contact angles being 60° and 40° for graphene and the substrate, respectively. The dashed line is predicted by the continuum model. The breakdown of the continuum model is predicted at N = 1690 for Γ_{GS} = 0.242 (dotted vertical line in A) and N = 7640 for Γ_{GS} = 0.1 J/m^2.

Section 4: Properties of materials.

Table S1. Shear/sliding stress in 2D material interface

	G-SiO_2 (5, 34)	G-G (5)	HOPG-HOPG (35)	MoS_2-MoS_2 (36)	G-G	G-hBN	hBN-hBN
Shear stress (MPa)	0.5-3.0	0.02-0.06	0.02–0.04	0.04-0.12	MD simulations (37) Average: ~0		
Maximum $\bar{\tau}$*	10^{-4}–10^{-3}**	$< 10^{-4}$	$< 10^{-4}$	$\approx 10^{-4}$			

G denotes graphene; Blue region shows experimentally measured data; Yellow region shows simulations results, whose averages approach 0 due to their stick-slip friction with periodically changing peak shear stress.

*To estimate the maximum $\bar{\tau}$, we utilized the largest experimentally observed h/a (1.8) and the radius (~300 nm) as well as the highest shear stress in the third row and the lowest E_{2D} in Table S2. We conclude that for heterostrutures with atom-level smooth interface, we can safely use model with frictionless approximations where $\phi = 6/5$.

**For a typical graphene blister on SiO_2 with h/a of ~0.8 and the radius of 200 nm, the $\bar{\tau}$ is in the range from 0.0002 to 0.001. The used ϕ will cause little influence on the adhesion energy estimation since the contact angle part contributes to the Γ greatly.

Table S2. Average modulus of 2D materials			
	Graphene (38)	MoS_2 (39)	hBN (40)
E (TPa)	1.00	0.27	0.87
E_{2D}(N/m)	340	180	289

Table S3. Water contact angle (WCA) for 2D materials and substrates						
	G/HOPG(32, 41)	MoS_2(42)	hBN(43)	Ice(44)	CaF_2(45)	Mica(46)
WCA (^{o})	64	69	47	12	20	23
	SiO_2(47)	SiC(48)	Si(49)	Sapphire(50)	Al_2O_3(51)	V_2O_5(52)
WCA (^{o})	40	73	60	10	36	0
Note that the exact liquid contact angle is highly challenging to measure since it can be influenced by various surface treatments, treating times, surface roughness, as well as containment types and density. In fact, even for water contact angels, there still exits inconsistence in literatures, especially for water contact angels of 2D materials. Herein, we used most widely adopted water contact angles, which can allow further comparative studies.						

References

1. Ferrari AC*, et al.* (2006) Raman spectrum of graphene and graphene layers. *Physical review letters* 97(18):187401.
2. Buscema M, Steele GA, van der Zant HS, & Castellanos-Gomez A (2014) The effect of the substrate on the Raman and photoluminescence emission of single-layer MoS2. *Nano Research* 7(4):561-571.
3. Brennan CJ*, et al.* (2017) Out-of-Plane Electromechanical Response of Monolayer Molybdenum Disulfide Measured by Piezoresponse Force Microscopy. *Nano letters*.
4. Yue K, Gao W, Huang R, & Liechti KM (2012) Analytical methods for the mechanics of graphene blisters. *Journal of Applied Physics* 112(8):083512.
5. Wang G*, et al.* (2017) Measuring interlayer shear in bilayer graphene. *Phys Rev Lett* 119:036101.
6. Hencky H (1915) On the stress state in circular plates with vanishing bending stiffness. *Z. Math. Phys* 63:311-317.
7. Fichter W (1997) *Some solutions for the large deflections of uniformly loaded circular membranes* (National Aeronautics and Space Administration, Langley Research Center).
8. Wang P, Gao W, Cao Z, Liechti KM, & Huang R (2013) Numerical analysis of circular graphene blisters. *Journal of Applied Mechanics* 80(4):040905.
9. Zhang K & Arroyo M (2016) Coexistence of wrinkles and blisters in supported graphene. *Extreme Mechanics Letters*.
10. Landau LD, Kosevich A, Pitaevskii LP, & Lifshitz EM (1986) Theory of elasticity.
11. Lim CHYX*, et al.* (2013) A hydrothermal anvil made of graphene nanoblisters on diamond. *Nature communications* 4:1556.
12. Lim CHYX, Nesladek M, & Loh KP (2014) Observing High‐Pressure Chemistry in Graphene Blisters. *Angewandte Chemie International Edition* 53(1):215-219.
13. Vasu K*, et al.* (2016) Van der Waals pressure and its effect on trapped interlayer molecules. *Nature communications* 7.
14. Plimpton S (1995) Fast parallel algorithms for short-range molecular dynamics. *Journal of computational physics* 117(1):1-19.
15. Brenner DW*, et al.* (2002) A second-generation reactive empirical bond order (REBO) potential energy expression for hydrocarbons. *Journal of Physics: Condensed Matter* 14(4):783.
16. Abascal JL & Vega C (2005) A general purpose model for the condensed phases of water: TIP4P/2005. *The Journal of chemical physics* 123(23):234505.
17. Vega C & De Miguel E (2007) Surface tension of the most popular models of water by using the test-area simulation method. *The Journal of chemical physics* 126(15):154707.
18. Wang P, Liechti KM, & Huang R (2016) Snap transitions of pressurized graphene blisters. *Journal of Applied Mechanics* 83(7):071002.
19. Gao W, Xiao P, Henkelman G, Liechti KM, & Huang R (2014) Interfacial adhesion between graphene and silicon dioxide by density functional theory with van der Waals corrections. *Journal of Physics D: Applied Physics* 47(25):255301.
20. Yoon T*, et al.* (2012) Direct measurement of adhesion energy of monolayer graphene as-grown on copper and its application to renewable transfer process. *Nano letters* 12(3):1448-1452.
21. Cao Z*, et al.* (2014) A blister test for interfacial adhesion of large-scale transferred graphene. *Carbon* 69:390-400.
22. Koenig SP, Boddeti NG, Dunn ML, & Bunch JS (2011) Ultrastrong adhesion of graphene membranes. *Nature nanotechnology* 6(9):543-546.
23. Zong Z, Chen C-L, Dokmeci MR, & Wan K-t (2010) Direct measurement of graphene adhesion on silicon surface by intercalation of nanoparticles. *Journal of Applied Physics* 107(2):026104.

24. Ishigami M, Chen J, Cullen W, Fuhrer M, & Williams E (2008) Atomic structure of graphene on SiO2. *arXiv preprint arXiv:0811.0587*.
25. Vanin M*, et al.* (2010) Graphene on metals: A van der Waals density functional study. *Physical Review B* 81(8):081408.
26. Edelsbrunner H & Mücke EP (1994) Three-dimensional alpha shapes. *ACM Transactions on Graphics (TOG)* 13(1):43-72.
27. Stukowski A (2010) Visualization and analysis of atomistic simulation data with OVITO–the Open Visualization Tool. *Model. Simul. Mater. Sci. Eng* 18(1):015012.
28. Ma J*, et al.* (2011) Adsorption and diffusion of water on graphene from first principles. *Physical Review B* 84(3):033402.
29. Gao W, Liechti KM, & Huang R (2015) Wet adhesion of graphene. *Extreme Mechanics Letters* 3:130-140.
30. Werder T, Walther JH, Jaffe R, Halicioglu T, & Koumoutsakos P (2003) On the water− carbon interaction for use in molecular dynamics simulations of graphite and carbon nanotubes. *The Journal of Physical Chemistry B* 107(6):1345-1352.
31. Werder T, Walther J, & Koumoutsakos P (2002) Hydrodynamics of Carbon Nanotubes-Contact Angle and Hydrophobic Hydration. *Technical Proceedings of the Second International Conference on Computational Nanoscience and Nanotechnology-ICCN*, p 490493.
32. Kozbial A*, et al.* (2014) Understanding the intrinsic water wettability of graphite. *Carbon* 74:218-225.
33. Wang P, Gao W, Wilkerson J, Liechti KM, & Huang R (2017) Cavitation of water by volume-controlled stretching. *Extreme Mechanics Letters* 11:59-67.
34. Wang X, Tantiwanichapan K, Christopher JW, Paiella R, & Swan AK (2015) Uniaxial Strain Redistribution in Corrugated Graphene: Clamping, Sliding, Friction, and 2D Band Splitting. *Nano letters* 15(9):5969-5975.
35. Liu Z*, et al.* (2012) Observation of microscale superlubricity in graphite. *Physical review letters* 108(20):205503.
36. Li H*, et al.* (2017) Superlubricity between MoS2 Monolayers. *Advanced Materials*.
37. Li Y, Zhang W, Guo B, & Datta D (2017) Interlayer Shear of Nanomaterials: Graphene-Graphene, Boron Nitride-Boron Nitride and Graphene-Boron Nitride. *Acta Mechanica Solida Sinica*.
38. Lee C, Wei X, Kysar JW, & Hone J (2008) Measurement of the elastic properties and intrinsic strength of monolayer graphene. *science* 321(5887):385-388.
39. Bertolazzi S, Brivio J, & Kis A (2011) Stretching and breaking of ultrathin MoS2. *ACS nano* 5(12):9703-9709.
40. Falin A*, et al.* (2017) Mechanical properties of atomically thin boron nitride and the role of interlayer interactions. *Nature Communications* 8:ncomms15815.
41. Li Z*, et al.* (2013) Effect of airborne contaminants on the wettability of supported graphene and graphite. *Nature materials* 12(10):925-931.
42. Kozbial A, Gong X, Liu H, & Li L (2015) Understanding the intrinsic water wettability of molybdenum disulfide (MoS2). *Langmuir* 31(30):8429-8435.
43. Wu Y, Wagner LK, & Aluru NR (2016) Hexagonal boron nitride and water interaction parameters. *The Journal of chemical physics* 144(16):164118.
44. Knight CA (1967) The contact angle of water on ice. *Journal of colloid and interface science* 25(2):280-284.
45. Zhang X, Wang X, & Miller JD (2015) Wetting of selected fluorite surfaces by water. *Surface Innovations* 3(1):39-48.
46. Gong X, Kozbial A, & Li L (2015) What causes extended layering of ionic liquids on the mica surface? *Chemical Science* 6(6):3478-3482.

47. Alam A, Howlader M, & Deen M (2014) The effects of oxygen plasma and humidity on surface roughness, water contact angle and hardness of silicon, silicon dioxide and glass. *Journal of Micromechanics and Microengineering* 24(3):035010.
48. Kazakova O, Panchal V, & Burnett TL (2013) Epitaxial graphene and graphene–based devices studied by electrical scanning probe microscopy. *Crystals* 3(1):191-233.
49. Kissinger G & Kissinger W (1991) Hydrophilicity of silicon wafers for direct bonding. *physica status solidi (a)* 123(1):185-192.
50. Zhang D, Wang Y, & Gan Y (2013) Characterization of critically cleaned sapphire single-crystal substrates by atomic force microscopy, XPS and contact angle measurements. *Applied Surface Science* 274:405-417.
51. Santos FdP*, et al.* (2003) Superficial modifications in TiO2 and Al2O3 ceramics. *Materials Research* 6(3):353-357.
52. Lim HS, Kwak D, Lee DY, Lee SG, & Cho K (2007) UV-driven reversible switching of a roselike vanadium oxide film between superhydrophobicity and superhydrophilicity. *Journal of the American Chemical Society* 129(14):4128-4129.